Deep-subaqueous implosive volcanism at West Mata seamount, Tonga

Arran P. Murch[1,2], Ryan A. Portner[1], Ken H. Rubin[3], David A. Clague[4]

1 *Geology Department, San Jose State University, San Jose, California 95192, USA*

2 *Department of Geology and Paleontology, National Museum of Nature and Science, Tsukuba, Japan*

3 *Department of Earth Sciences, University of Hawai'i at Mānoa, Honolulu, HI, United States*

4 *Monterey Bay Aquarium Research Institute, Moss Landing, California 95039, USA*

Abstract

Deep subaqueous volcanic eruptions (>500 m below sea level (mbsl)) remain enigmatic due to a lack of visual observations and difficulty recreating ambient conditions in the lab. Eruptive activity at West Mata seamount in May 2009 remains one of two deep subaqueous eruptions to have ever been filmed. A distinct low-intensity eruptive style, termed bubble escape activity, was observed at Hades vent (1200 mbsl) characterised by the ascent and implosion of 0.2 - 1 m diameter volatile-filled vapor bubbles (Resing et al. 2011). Video of this volcanic activity is used to constrain simple numerical models and produce the first subaqueous eruption actualistic model driven by visual observations.

Bubble escape activity occurs in three stages defined by changing exsolved volatile and lava behaviour. During Stage 1, vapor bubble ascent in a magma filled conduit drives either ductile or brittle deformation of the lava surface at the vent, depending on the timescale of lava cooling prior to bubble escape activity. Fragmentation of the lava during Stage 2 culminates with the vapor bubble coming into direct contact with the ambient water. At this point, Stage 3, bubbles implode

through rapid condensation and contraction of the exsolved volatile phase, due to rapid heat loss from the vapor bubble to the ambient water.

Numerical modelling of exsolved volatile expansion during conduit ascent to vents across the ocean depth range has identified a transition in exsolved volatile expansion characteristics at 2 - 5 MPa. This transition would produce a fundamental change in eruption processes, from which the characteristics and depth range of deep and shallow end members of bubble escape activity are defined.

Bubble escape activity highlights implosive behavior driven by underpressure that develops during exsolved volatile contraction as a key, but often overlooked, component of both pyroclastic and effusive subaqueous volcanism across the entire ocean depth range. This stands in contrast to overpressure driving subaerial explosive eruptions. The fact that exsolved volatiles can expand, contract, or maintain an approximately constant volume in subaqueous volcanism also calls for the careful application of terminology (e.g. explosive) to describe subaqueous eruption processes.

1. Introduction

Marine volcanism accounts for 70% of eruptions on Earth (Crisp 1984). However, most submarine eruptions go undetected aside from shallow and/or large events that breach the surface (Morimoto and Ossaka 1955; Carey et al. 2014; Cas and Simmons 2018). Recently, geophysical instrumentation at cabled submarine observatories have allowed monitoring of submarine eruptions in unprecedented detail (e.g. Kelley et al. 2014). Despite these advances there is still insufficient data to develop quantitative models of pyroclastic submarine eruption styles (e.g. Rubin et al. 2012; Cas and Simmons 2018). This is in part due to the lack of direct visual observations, which has limited our understanding of submarine pyroclast-forming processes.

Current submarine eruption models are mostly developed from ancient exposed (Carlisle 1963; Dimroth and Demarcke 1978) and modern *in-situ* (Gill et al. 1990; Clague et al. 2000) volcaniclastic sequences, physical experiments (Büttner et al. 2002; Schmid et al. 2010), and numerical models (Head and Wilson 2003; Cahalan and Dufek 2020). However, significant uncertainty remains due to limited knowledge of environmental conditions during pyroclast generation, inability to reproduce ambient deep subaqueous conditions in the lab, and difficulty modelling without constraints from visual observations and measurements. Greater use of currently available and future visual observations is therefore critical.

Remotely operated vehicle (ROV) video observations from deep submarine eruptions at NW-Rota-1 in the Marianas Arc (~500 mbsl; Embley et al. 2006), and West Mata seamount in the NE Lau basin (~1200 mbsl; Resing et al. 2011) have solidified a paradigm shift in our understanding of deep-marine eruption styles. In this study, we present a new model of an implosive deep-marine pyroclast-forming eruption, termed *bubble escape activity*, during the 2009 West Mata eruption. ROV video observations are used to constrain numerical models of lava rheology, magma fragmentation, and exsolved volatile behaviour upon interaction with the ambient water column. However, data from seafloor samples are not used here since the material cannot be confidently linked to the specific eruption style in question. The resulting actualistic model, driven by real-time visual observations, is a first for a subaqueous eruption, helping refine our understanding of eruption dynamics.

2. Geological setting and the 2009 West Mata eruption

West Mata is located in the northeast Lau Basin, between the Tonga Trench and Lau back arc (Fig. 1a) (Embley et al. 2014; Chadwick et al. 2019). Its pre-2011 summit at 1159 mbsl rose from a base at ~2900 mbsl. West Mata erupts boninite (Resing et al. 2011), a hot, high magnesium, H_2O saturated andesite sometimes associated with nascent subduction zones (e.g. Dobson et al. 2006).

Volcanic activity was observed at the summit of West Mata in May 2009 during the NOAA-NSF funded NE Lau Event Response expedition aboard the R/V Thompson, TN271 (Resing et al. 2011), primarily using the ROV *Jason*. This activity was part of an eruption sequence that lasted from at least April 2007 to February 2011 (Embley et al. 2014; Chadwick et al. 2019). A regional hydrophone array recorded waxing and waning eruption intensity from January to May 2009, with the period of observation coinciding with a low in the sound intensity from West Mata (Resing et al. 2011).

The May 2009 eruption at West Mata originated from two vents named Hades (~1200 mbsl) and Prometheus (~1175 mbsl; Fig. 1b; Resing et al. 2011). Over five days of visual observation non-steady and steady eruption styles were observed from Hades and Prometheus vents, respectively. This study focuses on non-steady activity defined by the periodic release of 0.2-1 m diameter (Resing et al. 2011) lava-skinned bubbles, observed only at Hades vent. This eruption style is referred to here as *bubble escape activity*, and was accompanied by episodic diffuse gas venting and effusion of a 350-500 m long pillow lava flow. Hades vent and its associated flow were subsequently destroyed during the formation of a summit crater and mass wasting in 2010-2011 (Embley et al. 2014).

3. Methods

3.1 Video observations

Video was recorded by ROV *Jason* at 30 frames per second and *1920x1080* resolution using an inhouse camera produced by Advanced Imaging and Visualization Lab at Woods Hole Oceanographic Institution based on an Adimec 2000C camera with a Fujinon HA13 x 4.5BERD-S48 lens. Bubbles were outlined on each frame using Adobe Illustrator®, and binary images were measured in ImageJ (Schneider et al. 2012). Absolute measurements were not possible due to obscuration of the ROV laser scale by incandescent lava. Therefore, bubble area and height-above-vent measurements were made in pixels and normalized to the maximum values of individual

bubble escapes. This approach yields dimensionless values with maximum bubble area or height-above-vent being 1, and removes variation from differences in camera zoom or distance from the vent between different bubble escapes. In addition, measurements were only conducted when the ROV was approximately stationary for a complete bubble escape. To ensure accuracy bubble height-above-vent was only measured when the ROV was approximately level with the vent. See supplementary material A for a graphical explanation.

3.2 Calculating magma viscosity

Due to uncertainty in the crystal content, magma viscosity (η) was calculated using observations of lava deformation. Using equations (8) and (9) from James *et al*. (2008), equations 1 and 2 here, η and conduit radius (r_c) were varied to fit bubble terminal ascent rate (U_s) to the maximum and minimum bubble ascent rates measured in Stage 1,

$$U_s = Fr\sqrt{g2r_c} \quad \text{(equation 1)}$$

where g is acceleration due to gravity, and Fr is the Froude number given by

$$Fr = 0.345\left(1 - e^{-N_f/34.5}\right) \quad \text{(equation 2)}$$

and N_f is the inverse viscosity

$$N_f = \rho 2{r_c}^{3/2} g^{1/2}/\eta \quad \text{(equation 3)}$$

where ρ is liquid magma density, 2600 kg m^{-3} (Heap et al. 2020). Bubble radii (r_b) of 0.1 to 0.5 m have been estimated by Resing *et al.* (2011), η was therefore calculated using a r_b of 0.5 m for the maximum U_s and of 0.1 m for the minimum U_s:

$$r_b = r_c - \sqrt[3]{3\eta r_c U_s/2\rho g} \quad \text{(equation 4)}$$

An eruption temperature (T_e) of 1155 °C is based on the approximate median for the estimated range of Bonin Island boninites (from two-pyroxene geothermometry; Dobson et al. 2006).

118 The lack of an absolute scale introduces major uncertainties into measurements of ascent
119 rate and therefore also on viscosity estimates (Equations 1-4). In the analysis presented here we are
120 therefore limited to discussion of data from the entire bubble population and cannot conduct
121 comparisons between bubble escapes.

122 *3.3 Bubble Expansion Model*

123 Vapor bubble expansion during isothermal decompression in the final 100 m of ascent to a
124 vent at water depths of 0-4000 mbsl is calculated using a 1-D numerical model outlined in James *et*
125 *al.* (2008). The model presented by James *et al.* (2008) is a simplified 1-D numerical model of a single
126 gas bubble rising through a liquid filled tube that solves for both the height of an expanding bubble's
127 nose and the height of the liquid surface over time. These are solved as a function of liquid density
128 and viscosity, bubble and conduit size, and ambient surface pressure. A full list of initial values is
129 given in supplementary material B.

130 *3.4 Thermal model*

131 A 1-D transient heat conduction model with forced convective heat loss through the surface
132 (after Schiesser 1991; Buttsworth 2001) is used to calculate heat loss from lava in contact with
133 ambient water using python code from (Clarke *et al*. 2019). For simplification, the lava is assumed to
134 be dense with no permeability and the model therefore gives a minimum estimate of heat loss.
135 Using major element compositions and measured dissolved H_2O contents of 0.90 to 0.94 wt%
136 (Resing et al. 2011), the thickness of the quenched rim in the cooling lava is calculated using a
137 constant glass transition temperature (T_g) of 830 ^oC after Giordano *et al.* (2008), assuming a cooling
138 rate of 10 K s^{-1}. Additional details and input parameters are in supplementary material C.

139 *3.5 Calculating strain rate during bubble escape*

140 Strain (ε) is calculated as the change in lava bubble wall volume during deformation (ΔV)
141 over the pre-deformation lava bubble wall volume (V_0). For simplicity, a constant bubble wall

thickness (*d*) of 2 cm was assumed. The pre-deformation lava bubble wall volume is estimated as the volume of a thin cylinder (disc) with a radius, r_1, equal to that of the rising vapor bubble, and a height of *d*. The volume of the domed lava bubble wall (V_d) is calculated as the difference between the volume of the dome encompassed by the lava bubble wall (V_1) and by the ascending vapor bubble (V_2). V_1 and V_2 are calculated using the equation for the volume of a spherical cap, the general form of which is;

$$V = \pi h^2/3\,(3r - h) \qquad \text{(equation 5)}$$

where *h* is the height of the spherical cap, and *r* is the radius of the sphere (i.e. the vapor bubble). When calculating V_1 and V_2 for both *h* and *r*, subscript 1 refers to the volume encompassed by the lava bubble wall, and subscript 2 refers to the vapor bubble, where $r_1 = r_2 + d$ and $h_1 = h_2 + d$. Strain is calculated by increasing *h* in steps to account for vapor bubble ascent to a maximum value occurring at $h = r_1$. Strain rate ($\dot{\varepsilon}$) can then be calculated using the measured vapor bubble ascent rates. By assuming a constant *d*, $\dot{\varepsilon}$ are maximum values since deformation will likely result in thinning of the bubble wall over time. See supplementary material D for a graphical explanation.

4. Results

4.1 The bubble escape sequence

Bubble escape activity is defined as the periodic escape of discrete vapor bubbles from a magma-filled conduit. The escape of a vapor bubble is split into three-stages based on changes in exsolved volatile and magma behavior together defined as a *bubble escape sequence* (Fig. 2). Bubble escape sequences typically occur in *bubble escape series*, with multiple rapid bubble escapes, over 0.2 to 4.9 s (Fig. 3). Series are separated by periods of quiescence 3 to 44 s long. In the following section the characteristics of each stage of the bubble escape sequence are described.

4.1.1 Stage 1 – Vapor bubble ascent

166 Stage 1 begins with ductile deformation of lava in the vent into a dome-shape, above an
167 ascending vapor bubble (Fig. 2a-b). The resulting lava bubble wall ductily deforms, and its pre-
168 existing quenched surface fractures into polygonal patches exposing underlying incandescent molten
169 magma (Fig. 4a-b). Quench-patches grow over time as exposed incandescent molten material is
170 cooled. Stretching of the lava bubble wall by the ascending vapor bubble continually exposes fresh
171 incandescent lava so an unbroken quenched surface does not develop. The vapor bubble remains
172 insulated from the ambient water by the lava wall throughout Stage 1, which ends when the wall
173 breaks and exposes the vapor to seawater (Fig. 4c).

174 The timescale of Stage 1 ranges from 0.033 to 0.899 s exhibiting a bimodal distribution with
175 peaks at ~0.1 and 0.4 s (Fig. 5c). The groups define long Stage 1A and short Stage 1B bubbles (Fig. 5a-
176 c). Stage 1A bubbles exhibit well-formed dome shaped lava bubble walls and slower rates of bubble
177 area increase (Fig. 5a). Stage 1B bubbles have faster rates of bubble area increase (Fig. 5b), and the
178 lava bubble wall breaks rapidly prior to the development of a dome shape (Fig. 6a-c).

179 Development of Stage 1A vs. 1B bubbles depends on the vent conditions during quiescent
180 pre-stage 1 (Fig. 3). Prior to a Stage 1A bubble lava extrusion is ongoing and the quenched surface at
181 the vent appears thin with cracks exposing underlying incandescent molten material. In contrast,
182 prior to a Stage 1B bubble no lava extrusion is apparent and the quenched surface appears thicker
183 with little to no incandescent lava visible (Fig. 6a).

184 Bubble ascent rates were calculated from measurements of bubble height-above-vent in
185 Stage 1 (Fig. 5d). At the maximum height-above-vent, vapor bubbles were roughly one diameter
186 above the vent (Fig. 2d). Assuming a bubble diameter of between 0.2 to 1 m (Resing et al. 2011),
187 ascent rates of ~0.13 to 1.3 m s^{-1} were estimated.

188 *4.1.2 Stage 2 – break-up*

189 Stage 2 begins when the vapor bubble is exposed to seawater upon lava wall break-up (Fig.
190 2c and 4c) and ends with initiation of vapor bubble contraction (Fig. 2c-d). Lava bubble wall breakup
191 begins with the formation of multiple tears in incandescent areas that quickly merge and propagate
192 to form a path for vapor bubble escape (Fig. 4a-f). Thin molten lava fibers were observed stretching
193 across a tear that opened over ~0.166 s (Fig. 4e). As the vapor bubble ascends, the void left in the
194 lava column behind it collapses (Fig. 2d). During Stage 2, vapor bubble area reaches a maximum
195 value (Fig. 5a-b). The time-scale of Stage 2 ranges from 0.067 to 0.366 s (Fig. 5c).

196 *4.1.3 Stage 3 - contraction*

197 Stage 3 is defined by rapid vapor bubble contraction starting with the formation of white
198 condensation clouds around the bubble margins (Fig. 7Ai-Bi). At the start of Stage 3 the vapor
199 bubble has an approximately spherical shape, with initially slow and symmetrical contraction.
200 However, ~0.133 s after the first condensation clouds develop, contraction becomes vertically
201 asymmetric as the bubble base rapidly contracts and inverts into a concave shape over ~0.033 to
202 0.066 s, while the top half of the vapor bubble retains a dome shape (Fig. 7Aii-Bii). A rapid inflow of
203 seawater upward towards the bubble base, marked by flow lines in the condensation clouds, forms a
204 mushroom shape vapor bubble (Fig. 7Aiii-Biii). During the latter part of Stage 3, contraction of the
205 top half of the vapor bubble coincides with the ejection of a vertical jet. The jet is observed through
206 the motion of the condensation cloud (Fig. 7Aiv and Biv), with an associated increase in measured
207 ascent rates (Fig. 5d). Jet formation coincides with the formation of a vortex ring and dispersal of
208 one or more partially-molten bombs (Fig. 2e-h), marking the end of Stage 3. Vapor bubble
209 contraction in Stage 3 lasts from 0.033 to 0.400 s (Fig. 5c). A buoyant turbulent plume formed after
210 Stage 3 disperses small pyroclasts and the condensation cloud, which remains visible in the water
211 column for >10 s, until it rises out of the field of view.

212

213 *4.2 Modelling*

To better understand the thermal and barometric effects of the ambient deep-marine environment on bubble escape activity, we construct simple models of thermal expansion and heat loss from exsolved volatiles and boninite lava when in contact with seawater at a range of depths.

4.2.1 Vapor expansion during magma ascent

Models of vapor expansion pre- and syn-Stage 1 assume isothermal conditions as vapor bubbles are isolated from cooling by the ambient marine environment. The water saturated state of boninite magma indicates H_2O is likely the dominate volatile species during the West Mata 2009 activity (Dobson et al. 2006). However, CO_2 is also considered here to make the results more generally applicable.

Vapor bubble expansion is calculated over the final 100 m of conduit ascent for vents between 0 and 4000 mbsl (0.101-40 MPa) using a 1-D numerical model outlined in James *et al.* (2008; Fig. 8a-b; supplementary material A). The model envisages the final 100 m of conduit ascent of a single large vapor bubble with an initial diameter (L_0) of 1 m, and an initial bubble pressure (P_0) equal to ambient pressure at 100 m depth in the conduit. P_0 is calculated using a liquid magma density of 2600 kg m^{-3} (Heap et al. 2020) and a water density of 1025 kg m^{-3} (Nayar et al. 2016). Magma viscosities of 60 to 180 Pa s at T_e (1155 ^oC) were estimated for conduit radii of 0.33 and 1.55 m, respectively, based on Stage 1 bubble ascent rates using bubble size estimates of 0.2 to 1 m (Resing et al. 2011). Estimated magma viscosities equate to crystal contents of 0.1 to 10% using the model of Giordano *et al*. (2008) and the Einstein-Roscoe equation (Lesher and Spera 2015), with bulk rock chemistry from Resing *et al.* (2011). Although this is lower than crystallinity estimates of 22 to 28% from the lava flow (Resing et al. 2011), the value here is derived directly from lava deformation behavior, and is therefore seen as more accurately describing the lava rheology.

A bubble expansion ratio for the final 100 m of conduit ascent is defined as the ratio of bubble diameter at the end of Stage 1 (L_e), over initial bubble diameter ($L_0 = 1$). Vapor bubble

238 diameter at the end of Stage 1 is measured when the difference between bubble head height and
239 lava surface height (i.e. thickness of the lava bubble wall) is <0.1 m (Fig. 8a).

240 Expansion ratios (L_e/L_0) for minimum and maximum magma viscosities and conduit radii plot
241 on top of each other across the full 0-4000 mbsl depth range (Fig. 8b). Two end member expansion
242 regimes are defined with a continuous transition at vent pressures of ~5 to 2 MPa (Fig. 8b). At vent
243 pressures higher than ~5 MPa (>500 m water depth) vapor bubble expansion in the final 100 m of
244 conduit ascent is small, with L_e/L_0 of 1.7 to 1.1. In contrast, at pressures lower than ~2 MPa (<200 m
245 water depth), expansion increases rapidly with decreasing pressure, with L_e/L_0 increasing from 2.1 at
246 2 MPa to 13.3 at 0.101 MPa (sea level; Fig. 8b). The expansion regime transition occurs at a
247 comparable pressure range with the change in H_2O and CO_2 specific volume (reciprocal of density)
248 during isothermal decompression (Fig. 8c; Zhang and Duan 2010; Lemmon et al. 2015).

249 *4.2.2 Vapor contraction during eruption*

250 Once the vapor bubble encounters ambient water it cools and contracts. Cooling occurs so
251 rapidly (Fig. 7), that an approximately constant pressure can be assumed. Cooling of H_2O and CO_2
252 from magmatic to ambient temperature at the ambient pressure of Hades Vent (~12 MPa) causes a
253 98% and 94% reduction in specific volume, respectively (Fig. 7c; Zhang and Duan 2010; Lemmon et
254 al. 2015). The majority of contraction occurs during and around phase changes in each exsolved
255 volatile species. At 12 MPa the phase transition from steam to water is instantaneous at 320 ^{o}C,
256 likely accounting for the bulk of vapor bubble contraction at West Mata. The transition from
257 supercritical fluid to liquid CO_2 is more gradual from ~130-30 ^{o}C. No equivalent data set for the
258 specific volume of other volatiles for the relevant pressure temperature conditions could be found.

259 *4.2.3 The effect of heat loss on lava rheology*

260 To understand the impact of quenching on lava rheology, heat loss to the ambient
261 environment is modelled during pre-stage 1 quiescence for Stage 1B bubbles, and during Stage 1A.

Heat loss analysis is not suitable during pre-stage 1A quiescence as lava extrusion provides a sustained source of heat preventing penetration of the cooling front.

The lack of visible lava extrusion, or incandescent molten material prior to Stage 1B bubbles suggests a relatively static conduit. Temperature profiles are calculated for a 10 m lava column with 200 µm steps from vent surface at 5, 10, 20, 30, and 40 s after contact with the water, with heat loss occurring through the vent, assuming insulated conduit margins. A quenched surface of 2.8, 3.9, 4.8, and 5.6 mm forms during periods of quiescence 10, 20, 30, and 40 s long, respectively (Fig. 9a). While penetration of the cooling front to 7.2, 10.2, 12.6, and 14.6 mm into the lava column over the same time produces a lower thermal gradient (~36 °C/mm), and a correspondingly broader rheological transition zone between the quenched rim and molten lava at T_e (Fig. 9a).

During Stage 1A the growth of quenched patches over the incandescent molten interior indicates the lava surface is cooling, however the bubble wall deformation style remains ductile. Here we calculate syn-eruption heat loss from a 2 cm thick lava bubble wall. Temperature profiles are calculated in 200 µm steps at 0.25, 0.5, 0.75, and 1 s after initial water contact (Fig. 9b). On the maximum bubble escape timescales of ~1 s, cooling is restricted to the outer 2 mm of the 2 cm thick lava bubble wall, forming a <0.7 mm thick quenched rim (Fig. 9b). The low penetration of cooling results in a high thermal gradient (~250 °C/mm) and a sharp rheological boundary between the quenched rim and bubble wall interior at T_e.

4.2.4 Magma rheology and bubble escape strain rates

By comparing estimated strain rate with the calculated glass transition, the rheological behavior of cooling lava during Stage 1 deformation can be approximated (Fig. 9c). The maximum strain rate of bubble escape activity at West Mata ranges from ~10^1 to 10^2 s^{-1}.

The glass transition was calculated using Maxwell's relation $\tau_r = \eta/G$ where τ_r is the Maxwell timescale, and *G* is the shear modulus, taken as ~10^{10} Pa (Dingwell and Webb 1989; Webb

and Dingwell 1990). The ductile-brittle transition (shown in blue Fig. 9c) occurs around two orders of magnitude below the relaxation rate (τ_r^{-1}), while the transition to shear thinning occurs approximately three orders of magnitude below τ_r^{-1} (Dingwell and Webb 1989; Webb and Dingwell 1990; Fig. 9c).

Differences in eruption processes during pre-stage 1A and 1B bubble quiescence results in two paths in temperature strain rate space, starting at the same initial conditions (Fig. 9c). Lava extrusion during pre-stage 1A quiescence restricts penetration of the cooling front. The lava thus remains dominantly at T_e, and will deform ductily in response to the strain rate applied in Stage 1, forming a domed lava wall (path A; Fig. 9c). In contrast, heat loss during pre-stage 1B quiescence cools a thicker layer of lava, producing a thicker brittle quenched rim underlain by cooled lava (path B; Fig. 9a). The strain rate applied in Stage 1 therefore induces brittle behavior, not only in the quenched rim, but also in the underlying lava cooled below ~750 to 850 ^{o}C (Fig. 9c). The thicker brittle layer in Stage 1B bubbles results in brittle fragmentation of the lava surface in response to strain from the ascending vapor bubble.

5. Discussion

5.1 Bubble escape activity

Bubble escape activity at West Mata is one of two deep subaqueous eruption styles to be observed in sufficient detail to generate an actualistic model of volcanic processes occurring at high hydrostatic pressure (Chadwick et al. 2008; Resing et al. 2011). In the following section, the impact of lava rheology and exsolved volatile behavior on eruption processes during a bubble escape sequence are discussed.

5.1.1 Magma Rheology

310 The effect of quenching on eruption processes during bubble release activity is highly
311 dependent on the timescale over which heat loss occurs. Lava has a low thermal conductivity (Lesher
312 and Spera 2015), meaning internal heat transfer is slow. As such, high heat transfer rates across a
313 magma water boundary (Schmid et al. 2010) only effect the surface of the lava, with the thermal
314 conductivity limiting deeper cooling (Fig. 9). The effect of quenching over different timescales can be
315 assessed by comparing the impact of heat loss on lava rheology over the bubble release sequence,
316 and during pre-Stage 1A, and pre-Stage 1B bubble quiescence (Fig. 9).

317 Heat loss on eruption timescales produces a thin and weak brittle quenched surface, with a
318 sharp, high thermal gradient contact with the underlying ductile bubble wall (Fig. 9b-c). Lava
319 deformation produces both brittle break-up of the quenched rim, and ductile deformation of the
320 molten interior (Fig. 2). However, the sharp rheological boundary between the quenched rim and
321 ductile interior acts as a barrier, limiting the impact each has on the behavior of the other (Fig. 9), as
322 suggested by bubble wall tears that only exist in the underlying incandescent molten lava (Fig. 4).
323 Therefore, during deformation the thin quenched rim breaks brittlely, but the overall lava rheology
324 is a function of the ductile interior.

325 Ejection of molten bombs at the end of Stage 3 further indicates that ductile behavior
326 dominates for cooling on eruption timescales (Fig. 10). The molten bombs are inferred to result from
327 the impact between ductile cavity walls that rush inward to fill the space left by the imploding vapor
328 bubble in Stage 3. This process forms a rapid vertical flow of molten lava (Gekle et al. 2009).
329 Stretching of the lava as it is ejected leads to its ductile break-up producing the bomb-sized
330 fragments expelled at the end of Stage 3 (Fig. 10).

331 Lava extrusion during pre-Stage 1A bubble quiescence continually replenishes hot material
332 at the vent (Fig. 3). The thermal and rheological profile of lava overlying the vent will thus be similar
333 to that generated on eruption timescales, with a thin quenched rim and sharp contact with the
334 underlying molten material (Fig. 9b). Deformation of the lava will therefore produce brittle breakup

335 of the quenched rim, while overall lava rheology is controlled by the ductile interior that forms a
336 domed bubble wall during Stage 1A (Fig. 2).

337 Prior to Stage 1B bubbles, longer cooling produces a thicker quenched rim and underlying
338 layer of pre-cooled, high viscosity lava, relative to pre-Stage 1A bubbles. Therefore, deformation by
339 the ascending pre-Stage 1B vapor bubble causes brittle break-up of the quenched rim and early
340 exposure of the vapor bubble to the ocean since underlying higher viscosity lava is unable to deform
341 ductily (Fig. 6). The thicker cooled layer between the quenched rim and ductile interior, formed by
342 longer term heat loss, therefore plays an important role in controlling the rheological behavior of
343 lava during Stage 1B bubble escape activity (Fig. 9).

344 These results question the inferred role of quenching in subaqueous volcanism as a key clast
345 forming process and controlling factor in magma rheology (van Otterloo et al. 2015), especially for
346 low-intensity clast forming eruptions in low viscosity magma (Clague et al. 2009). Data presented
347 here suggest that the timescale of heat loss is the key factor controlling the impact of quenching on
348 eruption processes. However, due to limitations from the video resolution this discussion is only
349 informed by lava deformation observed on the centimeter scale and larger.

350

351 5.1.2 Exsolved volatile behavior

352 *5.1.2.1 Ascent and non-expansion (Stage 1)*

353 During conduit ascent and Stage 1, the vapor bubble undergoes isothermal decompression
354 at T_e isolated from the ambient water by the lava (Fig. 10). The high ambient pressure, low viscosity
355 of the West Mata lava, and short time scale of Stage 1, preclude the build-up of overpressure from
356 exsolution that would drive a sudden expansion in the shallow conduit (Cashman and Sparks 2013).
357 Behavior of the exsolved volatile bubble prior to contact with ambient water can therefore be

358 explained by the expansion characteristics of the major exsolved volatile species (i.e. H_2O and CO_2)
359 under isothermal decompression.

360 Expansion of the vapor bubble during conduit ascent in Stage 1 is low, due to high ambient
361 pressures as is evident in the consistent bubble shape through Stage 1 (Fig. 2a-d, 4), and calculated
362 expansion ratios (Fig. 8b-c).

363 Limited expansion of exsolved volatiles at a depth of 1200 mbsl, and the lack of significant
364 bubble overpressure means there is no force driving 'explosive' expansion in the shallow conduit or
365 vent. Lava deformation and fragmentation is therefore driven by the vapor bubble's buoyant
366 momentum, resulting from over-stretching of the lava bubble wall of an ascending vapor bubble
367 undergoing negligible expansion (Fig. 10).

368 *5.1.2.2 Water contact and initial cooling (Stage 2)*

369 The vapor bubble does not immediately contract upon contact with the ambient water, but
370 maintains a consistent size through Stage 2 (Fig. 2c-d). The start of vapor bubble contraction is
371 marked by the formation of condensation clouds. These clouds are likely formed by condensation of
372 magmatic sulfur, the presence of which during the 2009 West Mata activity is shown by frozen sulfur
373 droplets adhering to the ROV on recovery and in proximal clastic samples. Sulfur condenses to liquid
374 droplets at a temperature >444 ^{o}C, which freeze between 115 and 153 ^{o}C (Young 1975). The
375 formation of condensation clouds at the start of Stage 3 indicates the temperature of the vapor
376 bubble during Stage 2 remains >444 ^{o}C. Cooling of H_2O and CO_2 from magmatic temperature to ~444
377 ^{o}C produces comparatively little contraction, as it is above the phase transitions for both species (Fig.
378 7c). Contraction during Stage 2 is therefore small, compared with the dramatic contraction observed
379 in Stage 3, likely resulting from H_2O condensation at ~320 ^{o}C (Fig. 10).

380 *5.1.2.3 Bubble implosion through asymmetric cavitation (Stage 3)*

Eruption processes during Stage 3 are driven by rapid contraction of the vapor bubble (Fig. 7), resulting from phase changes due to cooling by the ambient water (Fig. 7c). The formation of condensation clouds obscure visual observation of vapor bubble collapse processes (Fig. 2 and 6). However, features common to most vapor bubbles in Stage 3 point to the formation of a high-speed re-entry jet during contraction, suggesting a bubble collapse mechanism similar to asymmetric cavitation.

Asymmetric cavitation is a process where underpressure develops in a vapor bubble in a liquid causing it to collapse (e.g. Supponen et al. 2017). Deformation during vapor bubble contraction can cause one hemisphere to collapse faster, inverting and forming a high-speed re-entry jet. The impact of the re-entry jet on the opposite bubble wall generates large shockwaves and leaves a torus shaped remaining bubble (Plesset and Ellis 1958; Pecha and Gompf 2000; Supponen et al. 2017). The motion of the high-speed re-entry jet through the torus-shaped bubble forms a vortex ring ejected in the direction of the jet (Lauterborn 1982). Compression of the remaining torus-shaped vapor bubble continues until the in-rushing fluid rebounds forming a series of secondary shock waves (Supponen et al. 2017).

Stage 3 bubble collapses are asymmetric with the lower hemisphere becoming concave (Fig. 7). Asymmetric bubble collapse during Stage 3 is likely caused by deformation of the vapor bubble from its vertical movement, and proximity to the lava surface (Supponen et al. 2017). Inversion of the lower hemisphere is associated with the formation of flow lines in the condensation clouds indicating a rapid flow of water develops into the now concave bubble base (Fig. 7Aii-Biii). At the end of Stage 3 a fast-moving jet is ejected vertically from the bubble head, followed by a vortex ring (Fig. 7Aiv-Biv). This suggests a high-speed re-entry jet formed from inversion of the bubble base, traversing the vapor bubble to impact its head in <0.1 s.

Asymmetric cavitation provides a mechanism to generate acoustic signals recorded proximally to Hades vent during bubble escape activity, associated specifically with bubble collapse

406 (Dziak et al. 2015). Experiments and numerical modelling have shown shock waves with peak
407 pressures at their source in the range of 100's MPa to 10's GPa form during asymmetric cavitation
408 (e.g. Plesset and Ellis 1958; Pecha and Gompf 2000; Supponen et al. 2017). These shock waves would
409 be recorded as a series of rapidly generated energetic hydroacoustic signals associated with the
410 bubble implosion.

411 Caution should be used for any direct correlation between bubble escape activity and
412 cavitation, as the initial conditions at West Mata lie well outside the range of bubble size and
413 ambient pressure for any cavitation model (e.g. Supponen et al. 2017). It is also unclear how bubble
414 collapse driven by thermal contraction of the vapor phase will affect cavitation processes. Bubble
415 collapse partially enveloped by fluid lava bubble walls will also likely act to dampen energy release
416 from cavitation (LeBlanc et al. 2013). Nevertheless, comparable initial circumstances, similarities in
417 observed processes, and consistency with recorded hydroacoustic signals suggests cavitation is an
418 appropriate model with which to discuss implosive activity in Stage 3.

419 For simplicity we have considered the escape of individual large vapor bubbles. However,
420 the majority of bubble escape series consist of multiple bubble escapes in rapid succession (Fig. 3),
421 pointing to a more complex reality where bubble escape activity is likely driven by closely packed
422 groups of large ascending vapor bubbles (Parfitt 2004). Despite the simplification, the dynamics of
423 bubble escape and collapse would remain consistent.

424 *5.2 The depth range of bubble escape activity*

425 The lack of visual observations and difficultly of determining water depth in ancient deposits
426 has made correlating different styles of subaqueous activity with water depth difficult (e.g. Carlisle
427 1963; Dimroth and Demarcke 1978). However, bubble escape activity is controlled primarily by the
428 thermal expansion characteristics of the exsolved volatile bubble. Therefore, through an
429 understanding of the effect of hydrostatic pressure on vapor thermal expansion characteristics,

changes in eruption style can be investigated, given similar magma compositions and eruption intensities (Fig. 8).

Vapor bubble expansion during isothermal decompression in Stage 1 is inversely related to ambient hydrostatic pressure, producing two end member expansion regimes: a deep low expansion regime, and a shallow high expansion regime (Fig. 8). In the deep low expansion regime, at vent pressures higher than 5 MPa (500 m water depth), vapor bubble expansion in the shallow conduit and during the transition to the water column is similarly restricted (Fig. 8b). As such, were the bubble escape activity observed at West Mata in 2009 to occur at *any* water depth greater than 500 m, the behavior of an ascending vapor bubble would remain fundamentally the same (Fig. 8). Theoretically, if volatiles were infinitely available for exsolution, there is no lower depth limit to this regime as both H_2O and CO_2 contract when cooled, even when supercritical (Fig. 8). However, at higher ambient pressures the higher solubility of H_2O means activity would likely be driven by CO_2, while vapor bubble size would be reduced (Clague et al. 2009).

In the shallow high expansion regime, at vent pressures less than 2 MPa (200 m water depth), shallow conduit vapor bubble expansion becomes increasingly significant (Fig. 8), meaning Stage 1 and 2 would become progressively dominated by bubble expansion as water depth became shallower. However, since vapor bubble contraction in Stage 3 is driven by rapid heat transfer, bubble collapse would still occur so long as the vapor bubble remains entirely underwater, irrespective of pressure (Fig. 7c). Bubble escape activity would only end once the vapor bubble breached the sea surface, allowing vapor to escape and expand before collapsing due to rapid heat loss in the water column.

Bubble escape activity as aa eruption mechanism is controlled by vapor expansion/contraction characteristics in a low viscosity lava (Fig. 10). As such the depth transitions defined here would not necessarily translate to every subaqueous eruption style. Higher viscosity lava would slow the ductile escape of exsolved volatile bubbles, while at higher volatile fluxes the

455 formation of a jet would prevent wholescale implosion of the volatile phase. Magma water
456 interaction could also induce expansion through heating of ambient water (Büttner et al. 2002).

457

458 *5.3 Implosive subaqueous volcanism*

459 Rapid collapse of the vapor bubble during Stage 3 points to a previously under-appreciated
460 style of volcanism we term implosive activity, which is restricted to the subaqueous environment
461 (Moore 1975; Portner et al. 2015). The rapidity of the vapor bubble collapse in Stage 3, along with
462 the formation of shock waves justifies use of the term implosion to describe this process. Indeed, the
463 lack of rapid expansion of the vapor bubble prior to contact with water means that no aspect of
464 bubble escape activity can be called explosive (Martin et al. 2000).

465 Volcanic implosions were described by Moore (1975), and although they have been largely
466 overlooked since, implosive behavior is likely a common feature of subaqueous eruptions that may
467 generate a notable pyroclastic fingerprint on the seafloor (Portner et al. 2015). Significant
468 contraction of both H_2O and CO_2 when cooled from magmatic to ambient temperatures (even at
469 supercritical conditions; Fig. 7c), and rapid heat transfer to the ambient water will quickly form large
470 underpressures. This means, wholescale implosion of the exsolved volatile phase is likely during
471 unsteady gas flux activity.

472 Since vapor implosion is dependent on rapid heat transfer, there is also no depth limit to
473 such behavior (Fig. 7c). Implosive behavior is therefore likely a key aspect even of shallow
474 subaqueous eruptions. For example, sea surface effects of shallow underwater explosion
475 experiments bear striking similarities to Surtseyan eruptions; first forming a spray dome, followed by
476 rooster tail jets, often with initial clean water jets followed by darker jets containing fragmented
477 material (e.g. Morimoto & Ossaka, 1955). Underwater explosion experiments have shown these
478 processes result from the explosive formation of a vapor bubble that subsequently rapidly expands

and contracts as it ascends through the water column, until it breaches the water surface or condenses (e.g. Costanzo, 2011). The similarities suggest the rapid cyclic expansion and contraction of an explosively generated vapor bubble ascending through shallow water maybe key in driving Surtseyan eruptions. This indicates the importance of implosive behaviour even for eruptions at only tens of meters water depth. Visual observations of collapsing pillow lavas and descriptions of concussive events painful for nearby divers also demonstrates energetic implosive behavior is not restricted to the collapse of large vapor bubbles during pyroclastic eruptions, but may also occur during purely effusive activity (Moore 1975).

Observations of implosive behavior here cover only the escape of individual large vapor bubbles from a low viscosity magma. It is less clear how implosive behavior might manifest in a higher viscosity lava, or for smaller rapidly emitted vapor bubbles. However, hydroacoustic evidence of bubble collapses (Dziak et al. 2012), along with observation of oscillatory behavior around the vent during subaqueous activity at NW Rota-1 (Embley et al. 2006; Chadwick et al. 2008), likely indicate some form of implosive activity occurred there too.

Oversight of implosions in subaqueous volcanism points to a lack of insight into the dynamic interaction between subaqueous volcanism and the ambient environment resulting from a dearth of visual observations (Moore 1975; Portner et al. 2015; Rubin et al. 2012; Cas and Simmons 2018). Future studies should consider implosions as a potential part of any subaqueous eruption model. Moving forward, acoustic signals generated by implosion of a vapor bubble, or pillow lava may also provide an important tool for studying and monitoring subaqueous volcanism (Dziak et al. 2012; Dziak et al. 2015).

6. Conclusions

Video observations of bubble escape activity at West Mata in 2009 offer a uniquely detailed window into a deep subaqueous pyroclast-forming eruption style. Results here demonstrate the dramatic impact of the ambient water column on eruption processes in the deep-sea environment, dominantly through the thermal expansion/contraction characteristics of exsolved volatiles. The high ambient pressure prior to contact between the exsolved vapor and ambient water means the overpressure driving explosive expansion in subaerial volcanic systems is essentially removed. As such it is inappropriate to apply the term 'explosive' to bubble escape activity, and perhaps also most other pyroclast-forming styles of deep-sea volcanism.

Instead, we conclude that significant magmatic underpressure during gas-charged marine volcanism can trigger implosive eruption styles. Rapid vapor cooling and contraction once in contact with the ambient water means implosive behavior is not only possible, but likely the norm, especially for eruptions with an unsteady gas flux. The strong control that thermal expansion/contraction characteristics of exsolved volatiles exert on processes during bubble escape activity can also give insight into changes in eruption style resulting from differing vent depths. For bubble escape activity end member deep and shallow expansion regimes are defined with a broad transition at ~5 to 2 MPa.

Acknowledgements

The National Science Foundation Ridge 2000 and the Margins programs, the NOAA Office of Ocean Exploration and Research, and the NOAA VENTS Program, supported expedition TN271, upon which this research is based. NSF grant OCE-0934278 supported D.A.C.'s participation on the cruise, and the David and Lucile Packard Foundation supported D.A.C.'s salary during and after the cruise to collect, process, and curate vitriclastic sediment samples. K.H.R. acknowledges NSF grants OCE-0929881 and OCE-1538121 for support of his participation in TN271, and subsequent expeditions as well as data collection, respectively. A.P.M and R.A.P. were supported by NSF grant OCE-1634044.

SOEST Publication Number 11428. All high-definition video was produced by the Advanced Imaging and Visualization Lab, copyright Woods Hole Oceanographic Institution. The authors would also like to thank two anonymous reviewers whose comments and feedback helped to greatly improve this manuscript.

Author contributions

DAC and KHR participated in expedition TN271 on which ROV video was collected. Analysis of the ROV video presented here was conducted by APM and RAP with contributions from both DAC and KHR. Modelling was conducted by APM and RAP. All authors were involved in discussion and interpretation of the data, and all authors contributed to the writing of the manuscript.

Figure captions

Fig. 1 – (a) Regional map showing the location of West Mata seamount in the northeast Lau Basin, *insert* is regional map indicating the location of West Mata seamount along the Tonga-Kermadec arc. (b) Detailed view of West Mata seamount showing the locations of Hades (H) and Prometheus (P) vents.

Fig. 2 – A set of video frames demonstrating the stages of a single bubble escape sequence. During Stage 1 (a and b) the lava bubble wall ductily domes over the ascending vapor bubble. In Stage 2 (c and d) the lava bubble wall tears, exposing the vapor bubble to the surrounding seawater. Rapid contraction of the vapor bubble occurs in Stage 3 forming condensation clouds (e and f). The end of Stage 3 is marked by the ejection of a molten bomb and is followed by heating of the ambient water along with an upward moving convective vortex ring (g and h). Upward momentum of the ring generates a convective thermal that entrains pyroclast fragments.

Fig. 3 – (a) A 20 second timespan showing three bubble escape series. The bubble areas of each sequence are normalized to the largest bubble of a series. The difference between a bubble release series and a bubble release sequence is marked in bubble escape series 4 (c and d). Active

551 lava extrusion continues throughout the entire 20 seconds considered here, including periods of
552 quiescence between series (b). Bubble escape series 2 is led by a long Stage 1A bubble escape
553 (circle), with short Stage 1B bubbles (triangles) following.

554 Fig 4 – Video frames showing lava bubble wall break-up from the end of Stage 1 (a) to the
555 start of Stage 2 (b-f). Tears always form in the underlying molten lava, (inset in c) and have little
556 effect on the overlying quenched patches. Fibers of molten lava can occasionally be observed
557 forming across opening tears in the molten lava bubble wall (insert in e). Tears in the molten lava
558 bubble wall cease to form once there is a path for the vapor bubble to escape (f).

559 Fig. 5 - Bubble area time series for long Stage 1a (a) and short Stage 1B (b) bubbles. The start
560 of Stage 2 and 3 are indicated by the orange and red circles respectively. (c) The length of each stage
561 measured for Stage 1A and 1B bubbles. (d) Normalized height-above-vent ($Height/Height_{max}$) vs.
562 time plots for three bubble escapes showing both bubble height during the bubble escape sequence
563 (filled circles) and condensation cloud height post Stage 3 (empty squares).

564 Fig. 6 – A sequence of frames showing a Stage 1B bubble escape. (a) prior to Stage 1 the lava
565 is overlain by a thick quenched crust with no lava extrusion. (b-c) the ascending vapor bubble during
566 Stage 1 cracks the quenched crust, (d) and the lava fragments soon after deformation exposing
567 vapor bubble to the ambient water. (e-g) contraction of the vapor bubble occurs rapidly starting
568 from the bubble base which rolls up into the bubble head forming a vertical jet. (h) A vortex ring
569 forms from the collapsing vapor bubble that disperses entrained fragments and the condensation
570 cloud.

571 Fig. 7 –Videos frames showing the Stage 3 collapse of the vapor bubble for two different
572 bubble escape sequences (A and B). (Ai and Bi) Vapor bubble collapse starts with initial slow
573 symmetric contraction and the start of condensation cloud formation. (Aii and Bii) Bubble
574 contraction becomes asymmetric and speeds up. (Aiii and Biii) Formation of condensation cloud
575 flows lines mark the ingress of seawater into the vapor bubble base. (Aiv and Biv) Bubble contraction

ends with the condensation of all visible vapor along with the ejection of a water jet from the bubble head, seen through the motion of the condensation clouds. (c) Exsolved volatile volume vs temperature at a pressure of 12 MPa for H_2O and CO_2 with phase changes indicated. Data for H_2O at temperatures <1000 ^oC and for CO_2 at <826 ^oC comes from Lemmon *et al.* (2015). Data for higher temperatures are from Zhang and Duan (2010).

Fig. 8 – (a) Results of numerical model from James *et al*. (2008), showing bubble expansion over the final 100 m of conduit ascent for vents at water depths of 0, 10, 50, 100, and 1200 (Hades vent) m. (b) Vapor bubble expansion ratios calculated for the final 100 m of conduit ascent using the results from the numerical model from James *et al*. (2008), for vent depths between sea level and 4 km water depth. Results from the maximum (blue dashed line) and minimum (red solid line) estimates of magma viscosity plot on top of each other. (c) Exsolved volatile specific volume (1/density) vs pressure under isothermal conditions for H_2O and CO_2 with phase changes indicated. Data from Zhang and Duan (2010).

Fig. 9 – Thickness of the quenched rim and cooling front calculated from heat loss modelling of a 10 m thick column of lava over the period of pre-stage 1 quiescence (a) and a 2 cm thick molten lava bubble wall over the period of Stage 1 (b). (c) Strain rate vs. temperature diagram showing the estimated conditions of lava deformation during Stage 1 bubble escape activity, where X_c is magma crystallinity. Path A and path B are calculated for the effect of quenching 2 mm below the contact surface between lava and seawater on Stage 1A and pre-stage 1B quiescence timescales respectively.

Fig. 10 – Schematic diagram outlining the proposed model for bubble escape activity. The exsolved volatile behavior, lava rheology, and any fragmentation is shown at each step along with the position of each Stage of the bubble escape sequence. Interpretative diagrams indicate the proposed eruption processes occurring throughout.

601 **References**

602 Büttner, R., Dellino, P., La Volpe, L., Lorenz, V., Zimanowski, B., Volpe, L. La, Lorenz, V., Zimanowski,
603 B., 2002. Thermohydraulic explosions in phreatomagmatic eruptions as evidenced by the
604 comparison between pyroclasts and products from Molten Fuel Coolant Interaction experiments. J.
605 Geophys. Res. Solid Earth 107, 1–14. https://doi.org/10.1029/2001JB000511

606 Buttsworth, D.R., 2001. A finite difference routine for the solution of transient one dimensional heat
607 conduction problems with curvature and varying thermal properties. Univ. Southerm Queensl. Fac.
608 Eng. Surv. Tech. Rep. 1–32.

609 Cahalan, R.C., Dufek, J., 2020. Explosive Submarine Eruptions: The Role of Condensable Gas Jets in
610 Underwater Eruptions. J. Geophys. Res. Solid Earth. https://doi.org/10.1029/2020jb020969

611 Carey, R.J., Wysoczanski, R., Wunderman, R., Jutzeler, M., 2014. Discovery of the largest historic
612 silicic submarine eruption. Eos (Washington. DC). 95, 157–159.
613 https://doi.org/10.1002/2014EO190001

614 Carlisle, D., 1963. Pillow Breccias and Their Aquagene Tuffs, Quadra Island, British Columbia. J. Geol.
615 71, 48–71. https://doi.org/10.1086/626875

616 Cas, R.A.F., Simmons, J.M., 2018. Why Deep-Water Eruptions Are So Different From Subaerial
617 Eruptions. Front. Earth Sci. 6, 1–21. https://doi.org/10.3389/feart.2018.00198

618 Cashman, K. V., Sparks, S.R.S.J., 2013. How volcanoes work: A 25 year perspective. Bull. Geol. Soc.
619 Am. 125, 664–690. https://doi.org/10.1130/B30720.1

620 Chadwick, W.W., Cashman, K. V., Embley, R.W., Matsumoto, H., Dziak, R.P., Ronde, C.E.J. De, Lau,
621 T.K., Deardorff, N.D., Merle, S.G., Chadwick, W.W., Cashman, K. V., Embley, R.W., Matsumoto, H.,
622 Dziak, R.P., de Ronde, C.E.J., Lau, T.K., Deardorff, N.D., Merle, S.G., Jr, W.W.C., Cashman, K. V.,
623 Embley, R.W., Matsumoto, H., Dziak, R.P., Ronde, C.E.J. De, Lau, T.K., Deardorff, N.D., Merle, S.G.,

624 2008. Direct video and hydrophone observations of submarine explosive eruptions at NW Rota-1
625 volcano, Mariana arc. J. Geophys. Res. Solid Earth 113, 1–23. https://doi.org/10.1029/2007JB005215

626 Chadwick, W.W., Rubin, K.H., Merle, S.G., Bobbitt, A.M., Kwasnitschka, T., Embley, R.W., 2019.
627 Recent Eruptions Between 2012 and 2018 Discovered at West Mata Submarine Volcano (NE Lau
628 Basin, SW Pacific) and Characterized by New Ship, AUV, and ROV Data. Front. Mar. Sci. 6, 1–25.
629 https://doi.org/10.3389/fmars.2019.00495

630 Clague, D. a., Davis, A.S., Bischoff, J.L., Dixon, J.E., Geyer, R., 2000. Lava bubble-wall fragments
631 formed by submarine hydrovolcanic explosions on Lō'ihi Seamount and Kīlauea Volcano. Bull.
632 Volcanol. 61, 437–449. https://doi.org/10.1007/PL00008910

633 Clague, D. A., Paduan, J. B., and Davis, A. S. (2009). Widespread strombolian eruptions of mid-ocean
634 ridge basalt. J. Volcanol. Geotherm. Res. 180, 171–188. doi:10.1016/j.jvolgeores.2008.08.007.

635 Clarke, B., Calder, E.S., Dessalegn, F., Fontijn, K., Cortés, J.A., Naylor, M., Butler, I., Hutchison, W.,
636 Yirgu, G., 2019. Fluidal pyroclasts reveal the intensity of peralkaline rhyolite pumice cone eruptions.
637 Nat. Commun. 10, 2010. https://doi.org/10.1038/s41467-019-09947-8

638 Costanzo, F.A., 2011. Underwater explosion phenomena and shock physics. Conf. Proc. Soc. Exp.
639 Mech. Ser. 3, 917–938. https://doi.org/10.1007/978-1-4419-9834-7_82

640 Crisp, J.A., 1984. Rates of magma emplacement and volcanic output. J. Volcanol. Geotherm. Res. 20,
641 177–211. https://doi.org/10.1016/0377-0273(84)90039-8

642 Dimroth, E., Demarcke, J., 1978. Petrography and Mechanism of Eruption of the Archean Dalembert
643 Tuff, Rouyn-Noranda, Quebec, Canada. Can J Earth Sci 15, 1712–1723. https://doi.org/10.1139/e78-
644 181

645 Dingwell, D.B., Webb, S.L., 1989. Structural relaxation in silicate melts and non-Newtonian melt
646 rheology in geologic processes. Phys. Chem. Miner. 16, 508–516.
647 https://doi.org/10.1007/BF00197020

Dobson, P.F., Blank, J.G., Maruyama, S., Liou, J.G., 2006. Petrology and geochemistry of boninite-series volcanic rocks, Chichi-Jima, Bonin Islands, Japan. Int. Geol. Rev. 48, 669–701. https://doi.org/10.2747/0020-6814.48.8.669

Dziak, R.P., Baker, E.T., Shaw, A.M., Bohnenstiehl, D.R., Chadwick, W.W., Haxel, J.H., Matsumoto, H., Walker, S.L., 2012. Flux measurements of explosive degassing using a yearlong hydroacoustic record at an erupting submarine volcano. Geochemistry, Geophys. Geosystems 13, 1–14. https://doi.org/10.1029/2012GC004211

Dziak, R.P., Bohnenstiehl, D.R., Baker, E.T., Matsumoto, H., Caplan-Auerbach, J., Embley, R.W., Merle, S.G., Walker, S.L., Lau, T.K., Chadwick, W.W., 2015. Long-term explosive degassing and debris flow activity at West Mata submarine volcano. Geophys. Res. Lett. 42, 1480–1487. https://doi.org/10.1002/2014GL062603

Embley, R.W., Chadwick, W.W., Baker, E.T., Butterfield, D. a, Resing, J. a, de Ronde, C.E.J., Tunnicliffe, V., Lupton, J.E., Juniper, S.K., Rubin, K.H., Stern, R.J., Lebon, G.T., Nakamura, K., Merle, S.G., Hein, J.R., Wiens, D. a, Tamura, Y., 2006. Long-term eruptive activity at a submarine arc volcano. Nature 441, 494–7. https://doi.org/10.1038/nature04762

Embley, R.W., Merle, S.G., Baker, E.T., Rubin, K.H., Lupton, J.E., Resing, J.A., Dziak, R.P., Lilley, M.D., Chadwick, W.W., Shank, T., Greene, R., Walker, S.L., Haxel, J., Olson, E., Baumberger, T., 2014. Eruptive modes and hiatus of volcanism at West Mata seamount, NE Lau basin: 1996-2012. Geochemistry, Geophys. Geosystems 15, 4093–4115. https://doi.org/10.1002/2014GC005387

Gekle, S., Gordillo, J.M., Van Der Meer, D., Lohse, D., 2009. High-speed jet formation after solid object impact. Phys. Rev. Lett. 102, 1–4. https://doi.org/10.1103/PhysRevLett.102.034502

Gill, J., Torssander, P., Lapierre, H., Taylor, R., Kaiho, K., Koyama, M., Kusakabe, M., Aitchison, J., Cisowski, S., Dadey, K., Fujioka, K., Klaus, A., Lovell, M., Marsaglia, K., Pezard, P., Taylor, B., Tazaki, K., 1990. Explosive Deep Water Basalt in the Sumisu Backarc Rift. Science (80-.). 248, 1214–1217.

672 Giordano, D., Russell, J.K., Dingwell, D.B., 2008. Viscosity of magmatic liquids: A model. Earth Planet.
673 Sci. Lett. 271, 123–134. https://doi.org/10.1016/j.epsl.2008.03.038

674 Head, J.W., Wilson, L., 2003. Deep submarine pyroclastic eruptions: Theory and predicted landforms
675 and deposits. J. Volcanol. Geotherm. Res. 121, 155–193. https://doi.org/10.1016/S0377-
676 0273(02)00425-0

677 Heap, M.J., Kushnir, A.R.L., Vasseur, J., Wadsworth, F.B., Harlé, P., Baud, P., Kennedy, B.M., Troll,
678 V.R., Deegan, F.M., 2020. The thermal properties of porous andesite. J. Volcanol. Geotherm. Res.
679 398, 106901. https://doi.org/10.1016/j.jvolgeores.2020.106901

680 James, M.R., Lane, S.J., Corder, S.B., 2008. Modelling the rapid near-surface expansion of gas slugs in
681 low-viscosity magmas. Geol. Soc. London, Spec. Publ. 307, 147–167.
682 https://doi.org/10.1144/sp307.9

683 Kelley, D.S., Delaney, J.R., Juniper, S.K., 2014. Establishing a new era of submarine volcanic
684 observatories: Cabling Axial Seamount and the Endeavour Segment of the Juan de Fuca Ridge. Mar.
685 Geol. 352, 426–450. https://doi.org/10.1016/j.margeo.2014.03.010

686 Lauterborn, W., 1982. Cavitation bubble dynamics - new tools for an intricate problem. Appl. Sci.
687 Res. 38, 165–178. https://doi.org/10.1007/BF00385946

688 LeBlanc, J., Ambrico, J., Turner, S., 2013. Underwater Implosion Mechanics: Experimental and
689 Computational Overview, in: Blast Mitigation: Experimental and Numerical Studies. pp. 1–364.
690 https://doi.org/10.1007/978-1-4614-7267-4

691 Lemmon, E.W., McLinden, M.O., Friend, D.G., 2015. Thermophysical properties of fluid systems. In:
692 Linstrom, P.J., Mallard, W.G. (Eds.), NIST Chemistry WebBook, NIST Standard Reference Database,
693 vol. 69. National Institute of Standards and Technology, Gaithersburg, MD, p. 20899.

694 Lesher, C.E., Spera, F.J., 2015. Thermodynamic and Transport Properties of Silicate Melts and
695 Magma, Second Edi. ed, The Encyclopedia of Volcanoes. Elsevier Inc. https://doi.org/10.1016/B978-
696 0-12-385938-9.00005-5

697 Martin, R.J., Reza, A., Anderson, L.W., 2000. What is an explosion? A case history of an investigation
698 for the insurance industry. J. Loss Prev. Process Ind. 13, 491–497. https://doi.org/10.1016/S0950-
699 4230(99)00082-0

700 Moore, J.G., 1975. Mechanism of Formation of Pillow Lava. Am. Sci. 63, 269–277.

701 Morimoto, R., Ossaka, J., 1955. The 1952-1953 Submarine eruption of the Myojin Reef near the
702 Bayonnaise rocks , Japan. Bull. Earthq. Res. Inst., Tokyo uni.

703 Nayar, K.G., Sharqawy, M.H., Banchik, L.D., Lienhard, J.H., 2016. Thermophysical properties of
704 seawater: A review and new correlations that include pressure dependence. Desalination 390, 1–24.
705 https://doi.org/10.1016/j.desal.2016.02.024

706 Parfitt, E. A. (2004). A discussion of the mechanisms of explosive basaltic eruptions. J. Volcanol.
707 Geotherm. Res. 134, 77–107. doi:10.1016/j.jvolgeores.2004.01.002.

708 Pecha, R., Gompf, B., 2000. Microimplosions: Cavitation collapse and shock wave emission on a
709 nanosecond time scale. Phys. Rev. Lett. 84, 1328–1330.
710 https://doi.org/10.1103/PhysRevLett.84.1328

711 Plesset, B.Y.M.S., Ellis, A.T., 1958. On the mechanism of cavitation damage. Wear 1, 455–456.
712 https://doi.org/10.1016/0043-1648(58)90222-9

713 Portner, R.A., Clague, D.A., Helo, C., Dreyer, B.M., Paduan, J.B., 2015. Contrasting styles of deep-
714 marine pyroclastic eruptions revealed from Axial Seamount push core records. Earth Planet. Sci. Lett.
715 423, 219–231. https://doi.org/10.1016/j.epsl.2015.03.043

716 Resing, J. a., Rubin, K.H., Embley, R.W., Lupton, J.E., Baker, E.T., Dziak, R.P., Baumberger, T., Lilley,
717 M.D., Huber, J. a., Shank, T.M., Butterfield, D. a., Clague, D. a., Keller, N.S., Merle, S.G., Buck, N.J.,
718 Michael, P.J., Soule, A., Caress, D.W., Walker, S.L., Davis, R., Cowen, J.P., Reysenbach, A.-L., Thomas,
719 H., 2011. Active submarine eruption of boninite in the northeastern Lau Basin. Nat. Geosci. 4, 799–
720 806. https://doi.org/10.1038/ngeo1275

721 Rubin, K.H., Soule, S.A., Chadwick Jr., W.W., Fornari, D.J., Clague, D.A., Embley, R.W., 2012. Volcanic
722 eruptions in the deep sea. Oceanography 25, 142–157. https://doi.org/10.5670/oceanog.2011.65

723 Schiesser. W. 1991. Heat conduction in cylindrical and spherical coordinates. The numerical method
724 of lines, 326. ISSN 1875-869X. https://doi.org/ 10.3233/HAB-2010-0222.

725 Schmid, A., Sonder, I., Seegelken, R., Zimanowski, B., Büttner, R., Gudmundsson, M.T., Oddsson, B.,
726 2010. Experiments on the heat discharge at the dynamic magma-water-interface. Geophys. Res.
727 Lett. 37, 2–5. https://doi.org/10.1029/2010GL044963

728 Schneider, C.A., Rasband, W.S., Eliceiri, K.W., 2012. NIH Image to ImageJ: 25 years of image analysis.
729 Nat. Methods 9, 671–675. https://doi.org/10.1038/nmeth.2089

730 Supponen, O., Obreschkow, D., Kobel, P., Tinguely, M., Dorsaz, N., Farhat, M., 2017. Shock waves
731 from nonspherical cavitation bubbles. Phys. Rev. Fluids 2.
732 https://doi.org/10.1103/PhysRevFluids.2.093601

733 van Otterloo, J., Cas, R.A.F.F., Scutter, C.R., Otterloo, J. Van, Cas, R.A.F.F., Scutter, C.R., 2015. The
734 fracture behaviour of volcanic glass and relevance to quench fragmentation during formation of
735 hyaloclastite and phreatomagmatism. Earth-Science Rev. 151, 79–116.
736 https://doi.org/10.1016/j.earscirev.2015.10.003

737 Webb, S.L., Dingwell, D.B., 1990. Non-Newtonian Rheology of Igneous Melts at High Stresses and
738 Strain Rates: Experimental Results for Rhyolite, Andesite, Basalt, and Nephelinite. J. Geophys. Res.
739 95, 15695–15701. https://doi.org/10.1029/JB095iB10p15695

Young, D., 1975. Phase diagrams of the elements. https://doi.org/10.2172/4010212

Zhang, C., Duan, Z., 2010. GFluid: An Excel spreadsheet for investigating C-O-H fluid composition under high temperatures and pressures. Comput. Geosci. 36, 569–572. https://doi.org/10.1016/j.cageo.2009.05.008

745

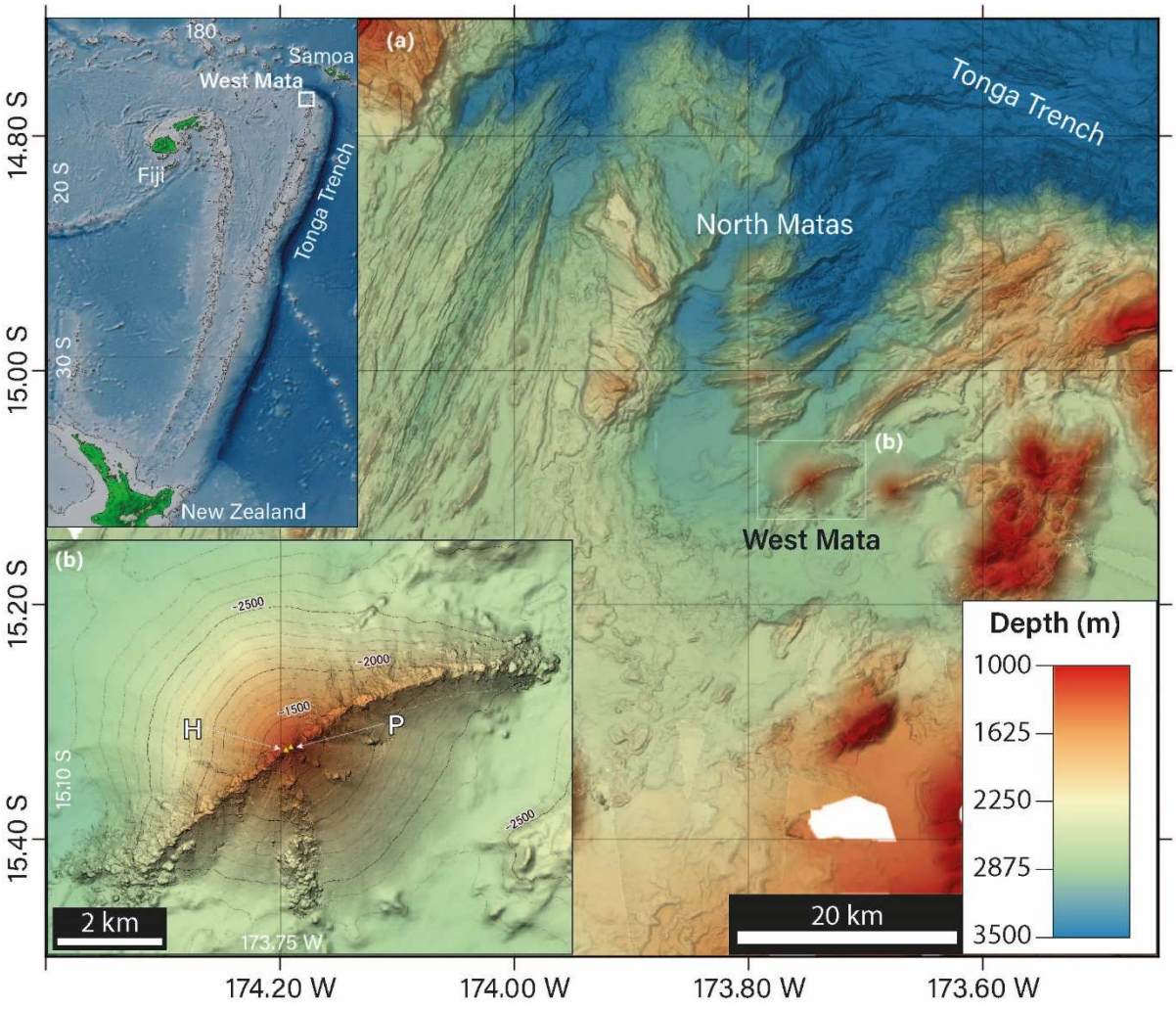

746

747 Fig 1

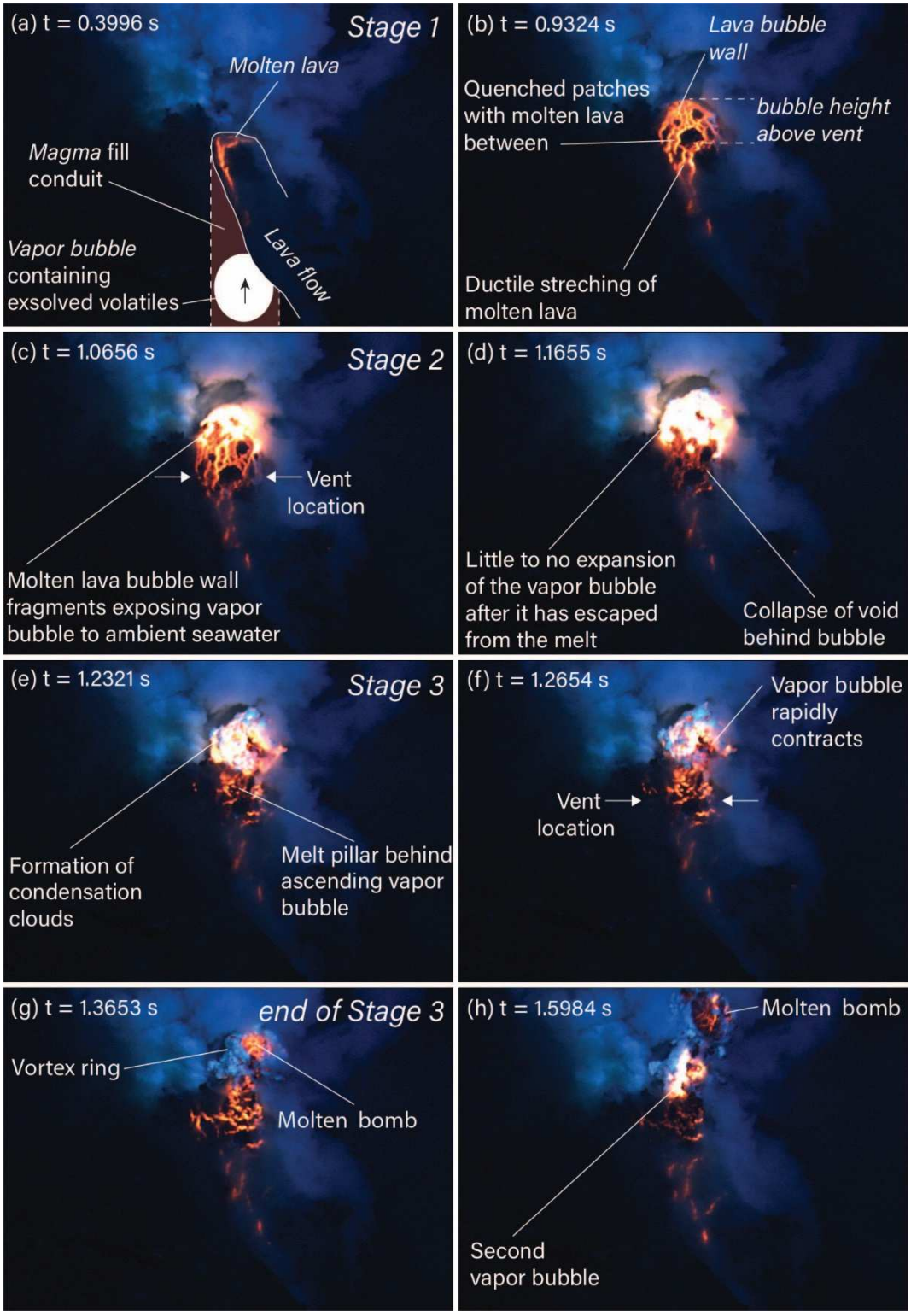
(a) t = 0.3996 s
Stage 1
Molten lava
Magma fill conduit
Vapor bubble containing exsolved volatiles
Lava flow
(b) t = 0.9324 s
Lava bubble wall
Quenched patches with molten lava between
bubble height above vent
Ductile streching of molten lava
(c) t = 1.0656 s
Stage 2
Vent location
Molten lava bubble wall fragments exposing vapor bubble to ambient seawater
(d) t = 1.1655 s
Little to no expansion of the vapor bubble after it has escaped from the melt
Collapse of void behind bubble
(e) t = 1.2321 s
Stage 3
Formation of condensation clouds
Melt pillar behind ascending vapor bubble
(f) t = 1.2654 s
Vapor bubble rapidly contracts
Vent location
(g) t = 1.3653 s
end of Stage 3
Vortex ring
Molten bomb
(h) t = 1.5984 s
Molten bomb
Second vapor bubble

748

749 Fig 2

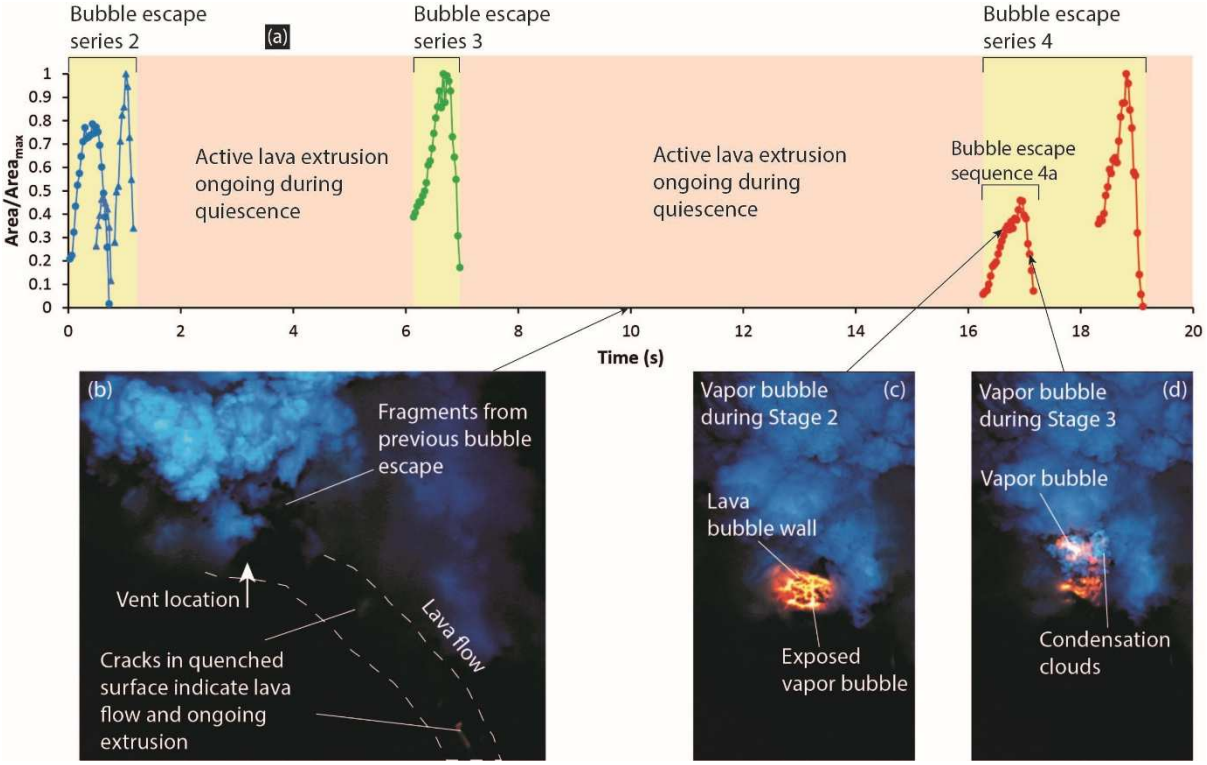
Bubble escape series 2
(a)
Bubble escape series 3
Bubble escape series 4
Active lava extrusion ongoing during quiescence
Active lava extrusion ongoing during quiescence
Bubble escape sequence 4a
Area/Area$_{max}$
Time (s)
(b)
Fragments from previous bubble escape
Vent location
Lava flow
Cracks in quenched surface indicate lava flow and ongoing extrusion
Vapor bubble during Stage 2
(c)
Lava bubble wall
Exposed vapor bubble
Vapor bubble during Stage 3
(d)
Vapor bubble
Condensation clouds

750

751 Fig 3

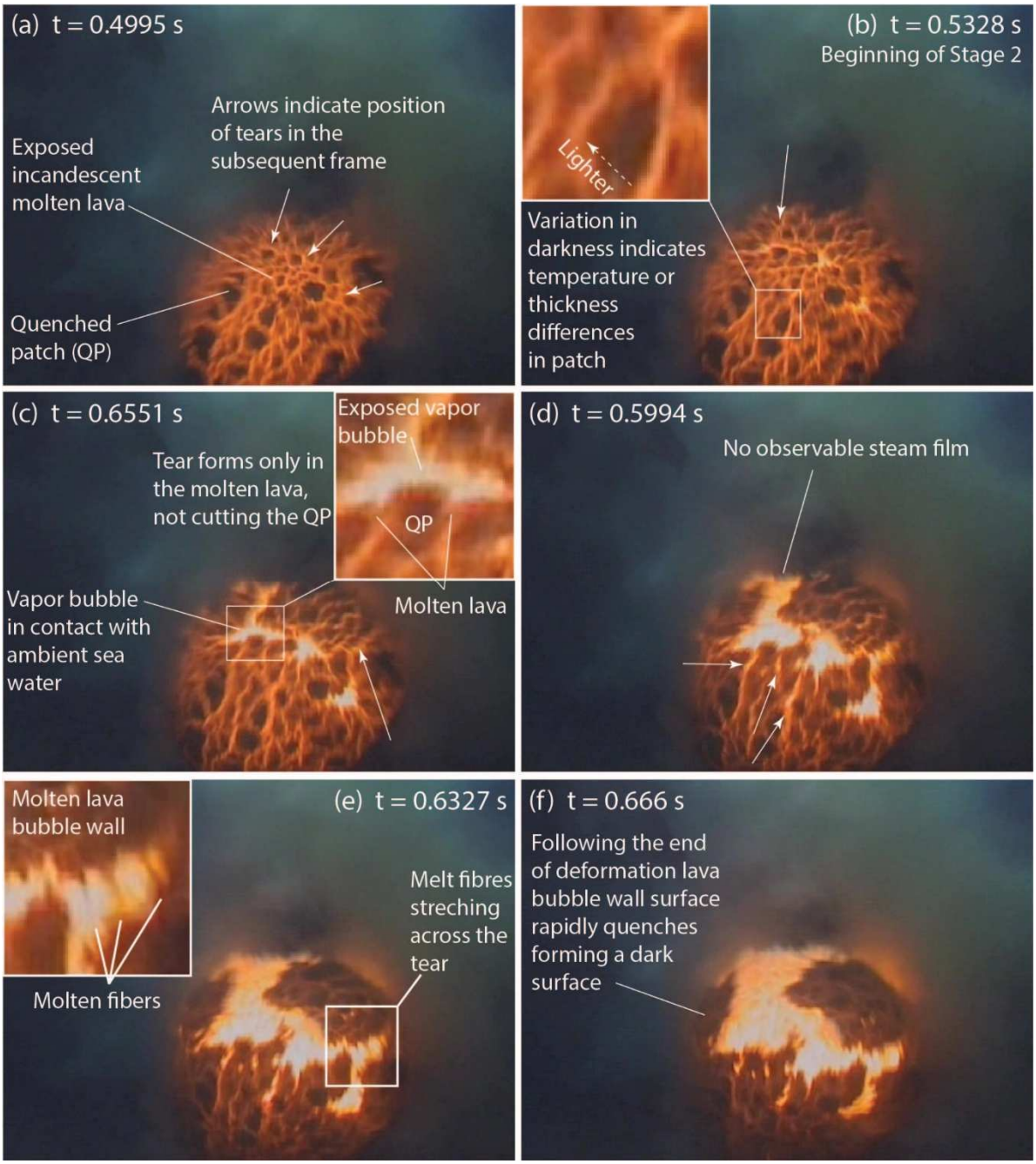
(a) t = 0.4995 s
Arrows indicate position of tears in the subsequent frame
Exposed incandescent molten lava
Quenched patch (QP)
(b) t = 0.5328 s
Beginning of Stage 2
Lighter
Variation in darkness indicates temperature or thickness differences in patch
(c) t = 0.6551 s
Exposed vapor bubble
Tear forms only in the molten lava, not cutting the QP
QP
Molten lava
Vapor bubble in contact with ambient sea water
(d) t = 0.5994 s
No observable steam film
Molten lava bubble wall
Molten fibers
(e) t = 0.6327 s
Melt fibres streching across the tear
(f) t = 0.666 s
Following the end of deformation lava bubble wall surface rapidly quenches forming a dark surface

752

753 Fig 4

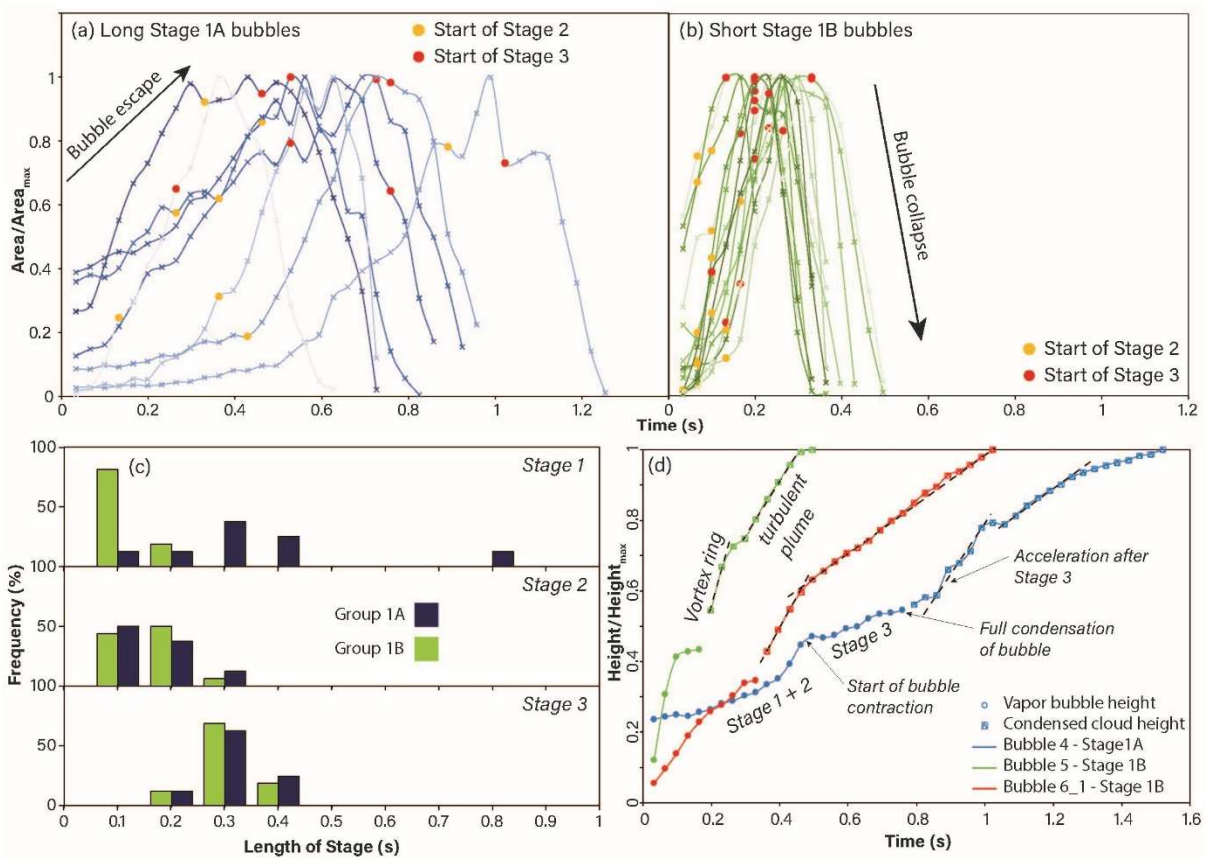
(a) Long Stage 1A bubbles
Start of Stage 2
Start of Stage 3
Bubble escape
Area/Area$_{max}$
(b) Short Stage 1B bubbles
Bubble collapse
Start of Stage 2
Start of Stage 3
Time (s)
(c)
Stage 1
Stage 2
Stage 3
Group 1A
Group 1B
Frequency (%)
Length of Stage (s)
(d)
Vortex ring
turbulent plume
Stage 1 + 2
Stage 3
Acceleration after Stage 3
Full condensation of bubble
Start of bubble contraction
Vapor bubble height
Condensed cloud height
Bubble 4 - Stage1A
Bubble 5 - Stage 1B
Bubble 6_1 - Stage 1B
Height/Height$_{max}$
Time (s)

754

755 Fig 5

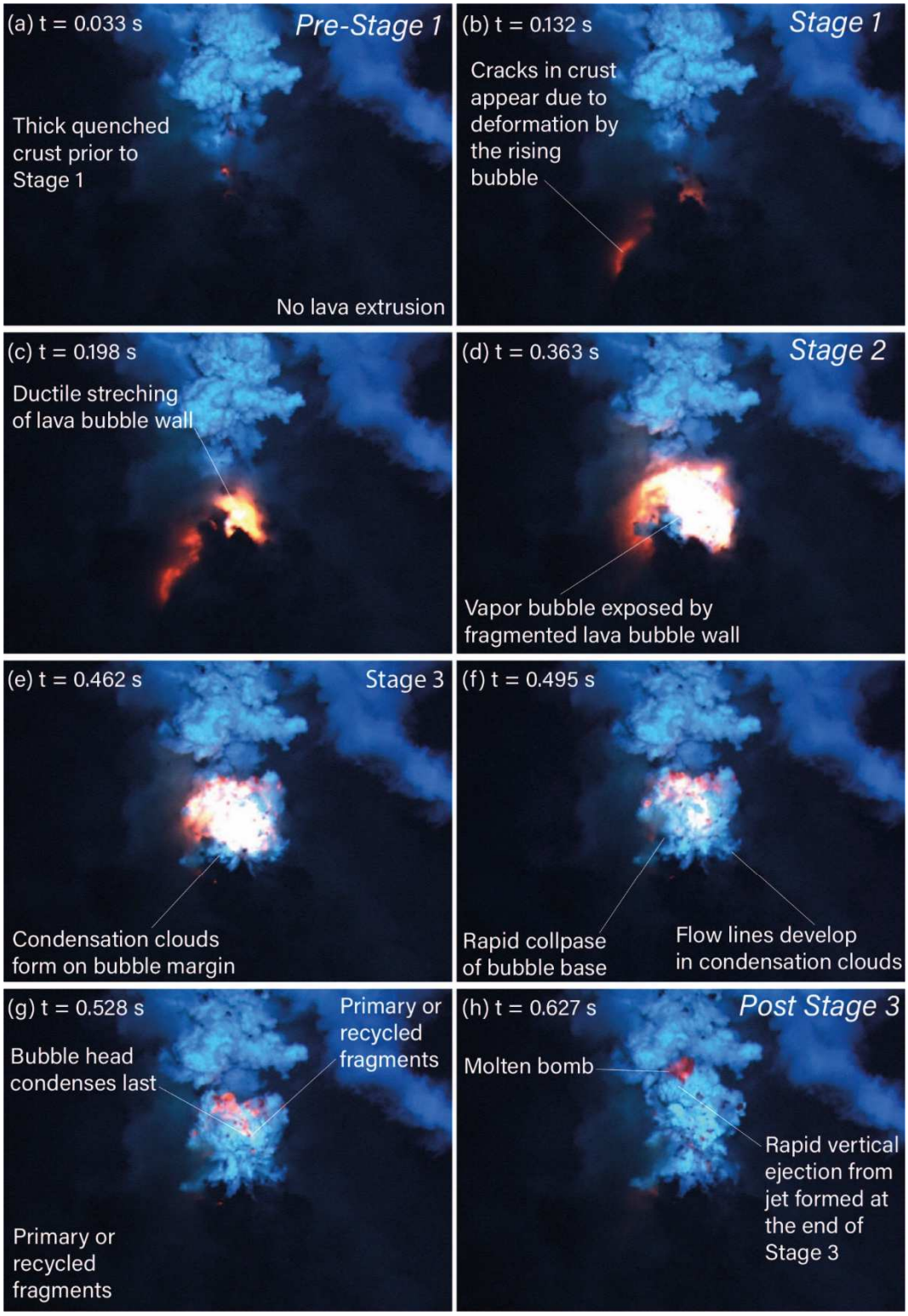
(a) t = 0.033 s
Pre-Stage 1
Thick quenched crust prior to Stage 1
No lava extrusion
(b) t = 0.132 s
Stage 1
Cracks in crust appear due to deformation by the rising bubble
(c) t = 0.198 s
Ductile streching of lava bubble wall
(d) t = 0.363 s
Stage 2
Vapor bubble exposed by fragmented lava bubble wall
(e) t = 0.462 s
Stage 3
Condensation clouds form on bubble margin
(f) t = 0.495 s
Rapid collpase of bubble base
Flow lines develop in condensation clouds
(g) t = 0.528 s
Primary or recycled fragments
Bubble head condenses last
Primary or recycled fragments
(h) t = 0.627 s
Post Stage 3
Molten bomb
Rapid vertical ejection from jet formed at the end of Stage 3

Fig 6

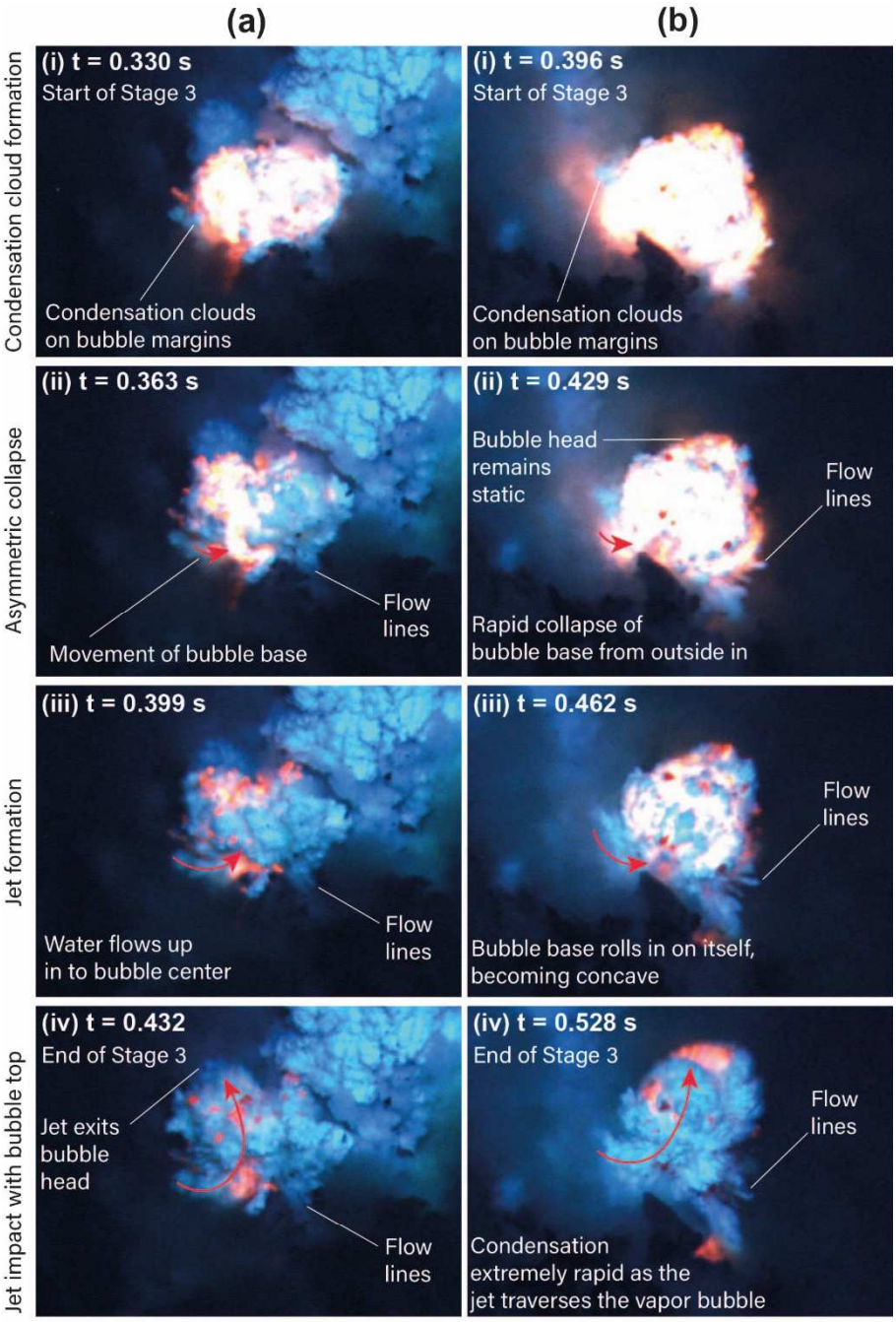
(a)
(b)
Condensation cloud formation
Asymmetric collapse
Jet formation
Jet impact with bubble top
(i) t = 0.330 s
Start of Stage 3
Condensation clouds on bubble margins
(i) t = 0.396 s
Start of Stage 3
Condensation clouds on bubble margins
(ii) t = 0.363 s
Movement of bubble base
Flow lines
(ii) t = 0.429 s
Bubble head remains static
Flow lines
Rapid collapse of bubble base from outside in
(iii) t = 0.399 s
Water flows up in to bubble center
Flow lines
(iii) t = 0.462 s
Flow lines
Bubble base rolls in on itself, becoming concave
(iv) t = 0.432
End of Stage 3
Jet exits bubble head
Flow lines
(iv) t = 0.528 s
End of Stage 3
Flow lines
Condensation extremely rapid as the jet traverses the vapor bubble
(c)
Isobaric - Pressure = 12 MPa
Vapor
H2O
CO2
Supercritical
Instantaneous volume change (condensation/boiling)
Liquid
Phase change
H2O 1155 to 5 °C = 98% vol decrease
CO2 1155 to 5 °C = 94% vol decrease
Volume (m3/kg)
0.1
0.01
0.001
0.0001
0
200
400
600
800
1000
1200
Temperature (°C)

759 Fig 7

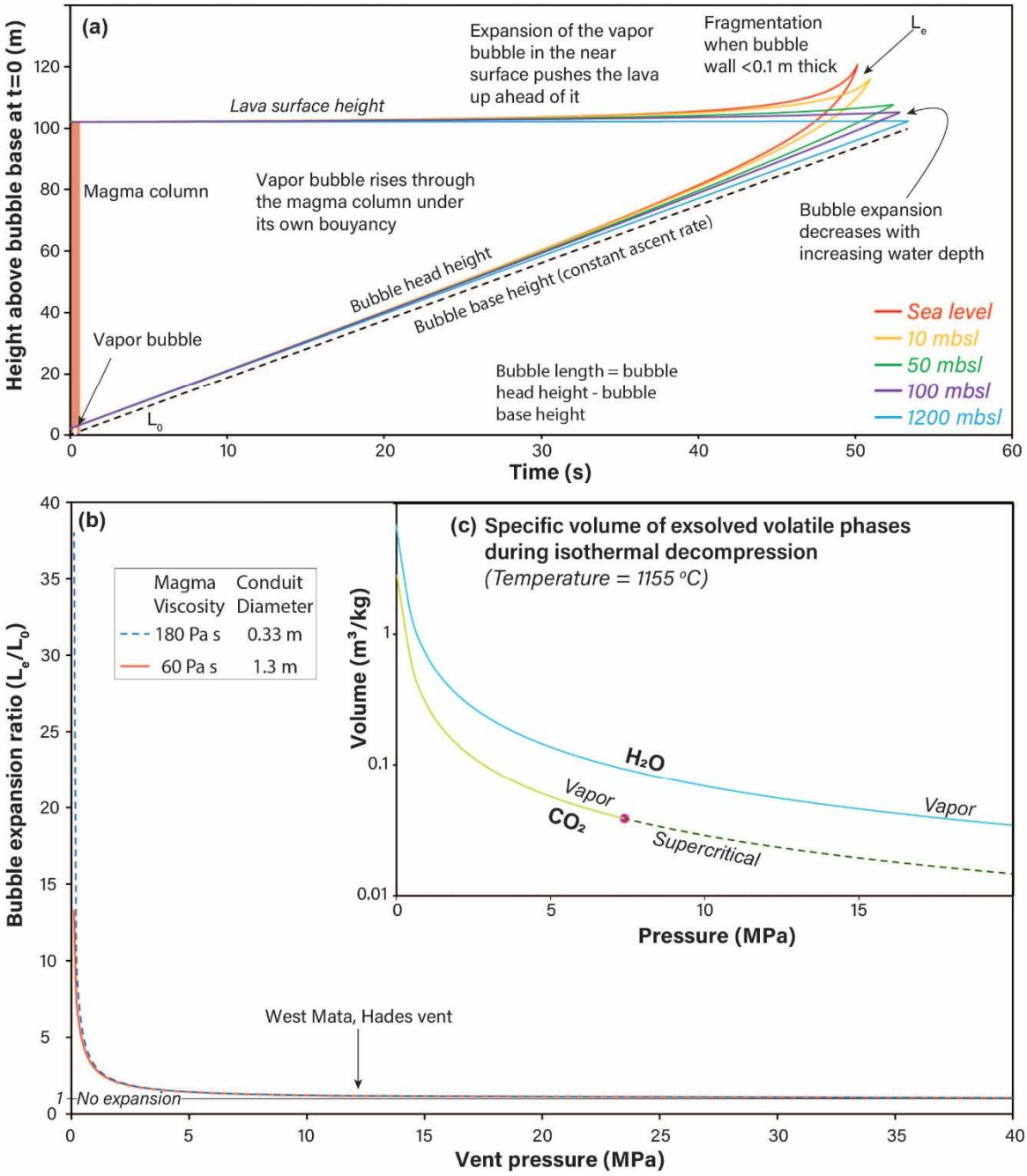

760

761 Fig 8

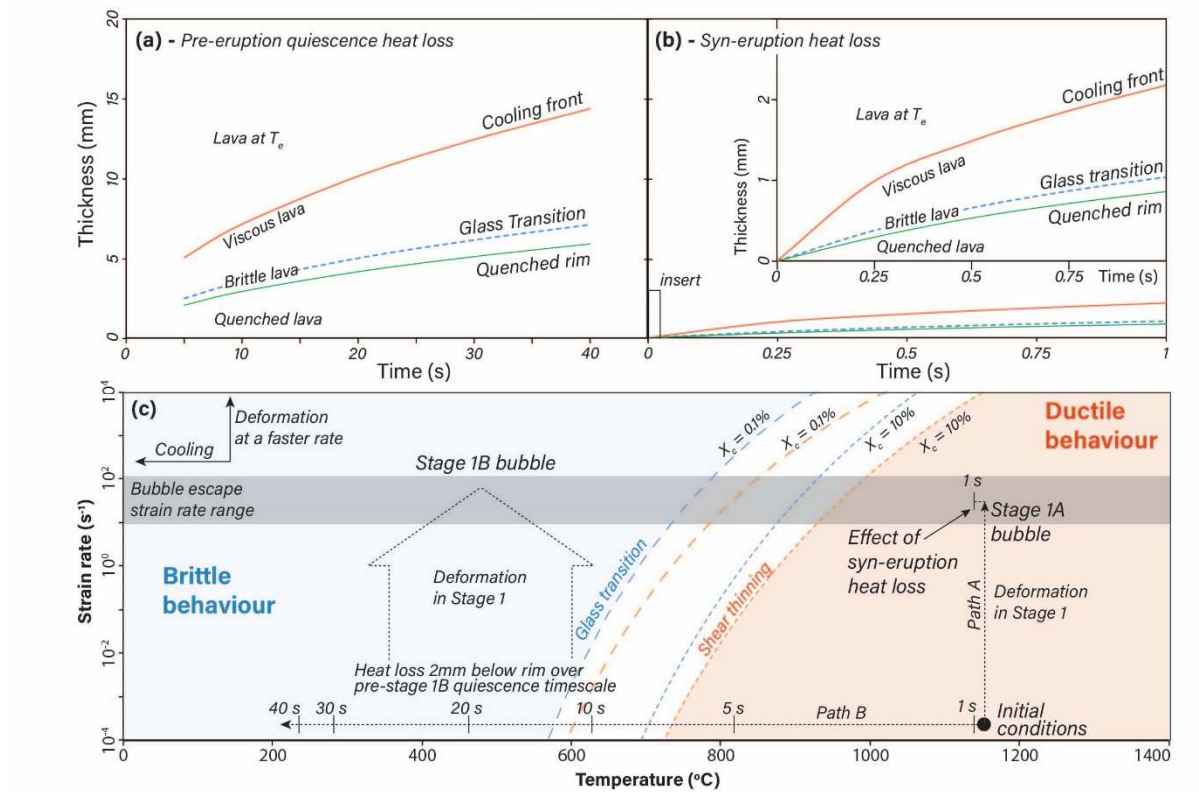
(a) - Pre-eruption quiescence heat loss
Thickness (mm)
Time (s)
Lava at T_e
Cooling front
Viscous lava
Glass Transition
Brittle lava
Quenched rim
Quenched lava
(b) - Syn-eruption heat loss
insert
Thickness (mm)
Time (s)
Lava at T_e
Cooling front
Viscous lava
Glass transition
Brittle lava
Quenched rim
Quenched lava
(c)
Deformation at a faster rate
Cooling
Stage 1B bubble
Bubble escape strain rate range
Brittle behaviour
Deformation in Stage 1
Heat loss 2mm below rim over pre-stage 1B quiescence timescale
Glass transition
Shear thinning
X_c = 0.1%
X_c = 0.1%
X_c = 10%
X_c = 10%
Ductile behaviour
1 s
Stage 1A bubble
Effect of syn-eruption heat loss
Path A
Deformation in Stage 1
40 s
30 s
20 s
10 s
5 s
Path B
1 s
Initial conditions
Strain rate (s^{-1})
Temperature (°C)

762

763 Fig 9

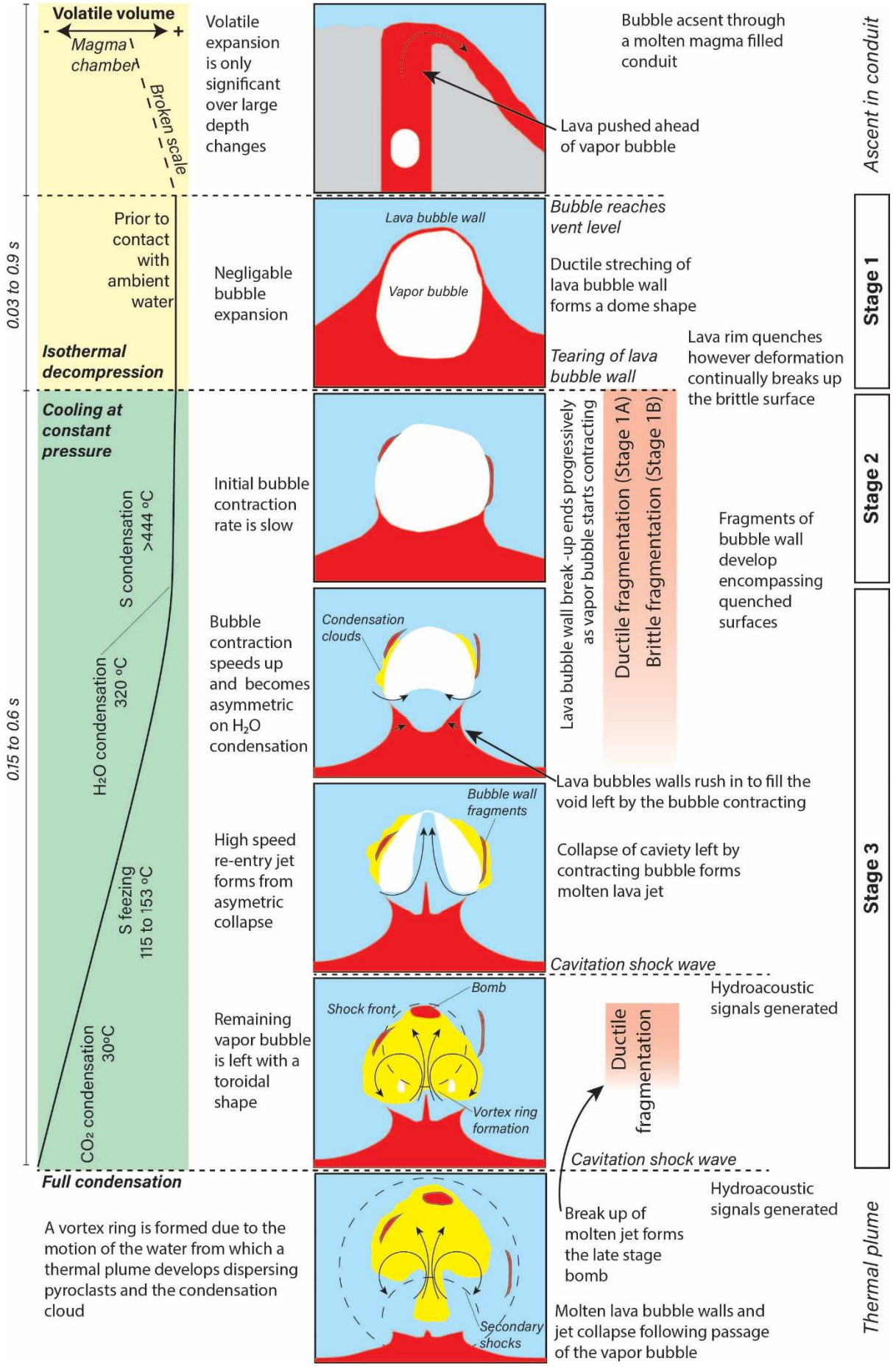
Volatile volume
Magma chamber
Broken scale
Volatile expansion is only significant over large depth changes
Bubble acsent through a molten magma filled conduit
Lava pushed ahead of vapor bubble
Ascent in conduit
0.03 to 0.9 s
Prior to contact with ambient water
Isothermal decompression
Negligable bubble expansion
Lava bubble wall
Vapor bubble
Bubble reaches vent level
Ductile streching of lava bubble wall forms a dome shape
Tearing of lava bubble wall
Lava rim quenches however deformation continually breaks up the brittle surface
Stage 1
Cooling at constant pressure
S condensation >444 °C
H2O condensation 320 °C
S feezing 115 to 153 °C
CO2 condensation 30°C
Initial bubble contraction rate is slow
Lava bubble wall break-up ends progressively as vapor bubble starts contracting
Ductile fragmentation (Stage 1A)
Brittle fragmentation (Stage 1B)
Fragments of bubble wall develop encompassing quenched surfaces
Stage 2
Condensation clouds
Bubble contraction speeds up and becomes asymmetric on H2O condensation
Lava bubbles walls rush in to fill the void left by the bubble contracting
0.15 to 0.6 s
Bubble wall fragments
High speed re-entry jet forms from asymetric collapse
Collapse of caviety left by contracting bubble forms molten lava jet
Cavitation shock wave
Hydroacoustic signals generated
Bomb
Shock front
Vortex ring formation
Remaining vapor bubble is left with a toroidal shape
Ductile fragmentation
Cavitation shock wave
Hydroacoustic signals generated
Stage 3
Full condensation
A vortex ring is formed due to the motion of the water from which a thermal plume develops dispersing pyroclasts and the condensation cloud
Break up of molten jet forms the late stage bomb
Secondary shocks
Molten lava bubble walls and jet collapse following passage of the vapor bubble
Thermal plume

765 Fig 10